



RESEARCH ARTICLE

10.1029/2020MS002180

Key Points:

- Global 0.56°-resolution data assimilation system was developed to integrate satellite observations of ozone, NO₂, CO, HNO₃, and SO₂
- The developed framework provides globally consistent analyses of emissions and concentrations on a megacity scale
- The data assimilation at 0.56°-resolution reduced errors against independent observations, which was larger than at lower resolutions

Correspondence to:

T. Sekiya,
tsekiya@jamstec.go.jp

Citation:

Sekiya, T., Miyazaki, K., Ogochi, K., Sudo, K., Takigawa, M., Eskes, H., & Boersma, K. F. (2021). Impacts of horizontal resolution on global data assimilation of satellite measurements for tropospheric chemistry analysis. *Journal of Advances in Modeling Earth Systems*, 13, e2020MS002180. <https://doi.org/10.1029/2020MS002180>

Received 12 MAY 2020

Accepted 28 APR 2021

Impacts of Horizontal Resolution on Global Data Assimilation of Satellite Measurements for Tropospheric Chemistry Analysis

Takashi Sekiya¹ , Kazuyuki Miyazaki² , Koji Ogochi¹, Kengo Sudo^{1,3}, Masayuki Takigawa¹ , Henk Eskes⁴, and K. Folkert Boersma^{4,5}

¹Japan Agency for Marine-Earth Science and Technology, Yokohama, Japan, ²Jet Propulsion Laboratory/California Institute for Technology, Pasadena, CA, USA, ³Graduate School of Environmental Studies, Nagoya University, Nagoya, Japan, ⁴Royal Netherlands Meteorological Institute (KNMI), De Bilt, the Netherlands, ⁵Meteorology and Air Quality Section, Wageningen University, Wageningen, the Netherlands

Abstract We present the results from a global 0.56°-resolution chemical data assimilation that integrates satellite observations of ozone, NO₂, CO, HNO₃, and SO₂ from OMI, GOME-2, SCIAMACHY, TES, MOPITT, and MLS. The assimilation is based on an ensemble Kalman filter technique and simultaneously optimizes ozone precursor emissions and concentrations of various species. The data assimilation at 0.56° resolution reduced model errors against independent surface, aircraft, and ozonesonde observations, which was larger than at coarser resolutions for many cases. By the data assimilation, surface model errors over major polluted regions were reduced by 33%–75% for NO₂ and by 15%–18% for ozone. Agreements against assimilated observations for NO₂ were improved using the data assimilation at 0.56° resolution by a factor of 1.5–3 compared to 2.8° resolution over major polluted regions. The estimated global total NO_x emission over medium and strong source areas were smaller by 15% at 0.56° resolution than at 2.8° resolution associated with resolving small-scale transport and chemistry processes, while 2%–26% smaller emissions were found for regional total emissions over Europe, the United States, China, India, and South Africa, with larger differences over megacities such as Los Angeles (–41%). The estimated ship emissions were 5%–7% smaller at 0.56° resolution over the Pacific and Atlantic. The 0.56°-resolution data assimilation provides globally consistent analyses of the emissions and concentrations on a megacity scale, which benefit studies on air quality and its impact on human health at various spatial scales over different regions of the world.

Plain Language Summary Air pollutants such as nitrogen oxides (NO_x) and ozone are important for air quality and climate change. This study demonstrates that global 0.56°-resolution data assimilation of multiple chemical species from multiple satellites can improve chemical concentrations of numerous key species including NO₂ and ozone, which was better than that at coarser resolutions. With the 0.56°-resolution data assimilation, improved agreements with independent surface, ozonesonde, and aircraft observations were obtained for many cases than at coarser resolutions. Over polluted areas, increasing horizontal resolution substantially impacts upon top-down NO_x emission estimates associated with nonlinear atmospheric transport and chemical processes. The globally consistent analyses of emissions and concentrations on a megacity scale obtained from the 0.56°-resolution data assimilation would benefit studies on air quality and its impact on human health at various spatial scales over different regions of the world.

1. Introduction

Nitrogen oxides (NO_x), carbon monoxide (CO), and sulfur dioxide (SO₂) are main precursors of tropospheric ozone and secondary inorganic aerosols, which are important for air quality and climate change (IPCC, 2013). Ozone, NO_x, and CO also affect oxidizing capacities through the ozone-HO_x-NO_x-CO-VOCs chemistry, which determines the lifetime of air pollutants and long-lived greenhouse gases, such as methane (e.g., Shindell et al., 2009). These air pollutants are highly emitted from significant energy use and other intensive human activities and enhanced on a megacity scale (e.g., 50 × 50 km²), which can resolve major megacities such as New York (9,882 km²), Paris (12,089 km²), Beijing (16,410 km²), and the Indian

National Capital Region (53,817 km²) (National Bureau of Statistics, 2018; National Capital Region Planning Board, 2016; OECD, 2012). The pollutants emitted from megacities can be transported over long distances (i.e., thousands of kilometer scales) and contribute to hemispheric background pollutions and global climate changes (e.g., Baklanov et al., 2016). In addition, the United Nations (2015) reported that the number of megacities is expected to rise globally including developing regions such as South and Southeast Asia, Africa, and Latin America. Pollutants are also emitted from natural sources including biomass burning, microbial activity in soil, lightning, and volcanic activity. Thus, globally consistent information on megacity-scale emissions and concentrations is important for various applications for air quality, its impact on human health, and climate change.

Spatial resolution of chemical transport model (CTM) based on Eulerian formulation has substantial effects on model simulation results through resolving emission distributions (Valari & Menut, 2008), nonlinear chemical processes (Valin et al., 2011; Wild & Prather, 2006), and meteorological fields which affects tracer transport, deposition, and photolysis and reaction rates (Klich & Fuelberg, 2014; Tie et al., 2010). High-resolution global modeling is also essential for Eulerian models to improve advection calculation of polluted plumes (Eastham & Jacob, 2017; Prather et al., 2008) and capture episodic deep intrusions from the stratosphere and their influence on near-surface ozone, including their inter-continental transports (M. Lin et al., 2012; Yamashita et al., 2017), through suppressing numerical diffusion at coarse resolutions. Lagrangian models do not suffer from numerical diffusion, while the use of Lagrangian models for global calculations has difficulties with accumulated errors in trajectories over time, heterogeneous coverages of air parcels after long time integration, and a lack of mixing with neighbor air parcels and subsequent nonlinear chemistry (e.g., Brasseur & Jacob, 2017).

Regional CTM studies (e.g., Tao et al., 2020; Tie et al., 2010; Valin et al., 2011) suggested that 5–15 km resolutions were necessary to improve ozone, aerosols, and their precursors at urban areas, while it is difficult to employ 5–15 km resolutions for the global domain due to limits on computational resources. Nevertheless, increasing resolution of global CTMs from 250–300 to 50–100 km greatly improved the model performance (e.g., Sekiya et al., 2018; Stock et al., 2014; Wild & Prather, 2006; Williams et al., 2017). The 50 km-bin grid size is comparable to or smaller than the total metropolitan areas of major mega cities, as mentioned above.

In addition, bottom-up emission estimates based on emission inventories have been regarded as a major uncertainty of CTM simulations, reflecting inaccurate emission factors and activity rates, for example, traffic rush hours and winter building heating (Streets et al., 2003), and incomplete knowledge of biomass burning emission factors for various situations (Castellanos et al., 2014). Top-down emission estimates, which is constrained by observational information using data assimilation and emission inversion techniques, have provided up-to-date information complementary to the bottom-up emission estimates at various spatial scales, especially over developing regions where information on activity and emission factors is less available (Elguindi et al., 2020; Streets et al., 2013). Global NO_x emission estimates were obtained at relatively low resolutions (1°–4°) using single-constituent inversion framework (Jaegle et al., 2005; Lamsal et al., 2011) and our multi-constituent data assimilation framework (e.g., Miyazaki & Eskes, 2013; Miyazaki et al., 2017). Nevertheless, top-down estimates have limitations and uncertainties associated with model representations of transport and chemical processes (e.g., Miyazaki, Bowman, Yumimoto, et al., 2020; Stavrakou et al., 2013). The multiconstituent data assimilation simultaneously optimizes the ozone precursor emissions and concentrations of various species and reduces model errors unrelated to emissions (e.g., the NO₂ chemical loss rate) (Miyazaki et al., 2017; Qu et al., 2019; Zheng et al., 2019). High-resolution top-down emission estimates (typically at 1–50 km resolution) can also reduce errors unrelated to emissions through resolving small-scale transport and chemical processes and improve emission estimates, while regional emissions inversion studies mainly focused on selected major polluted regions such as Europe, the United States, and East Asia (Ding et al., 2015; J.-T. Lin et al., 2010; X. Liu et al., 2017; Sourì et al., 2018).

Advanced data assimilation techniques, such as four-dimensional variational method (4D-Var) and ensemble Kalman filter (EnKF), can optimize pollutants' concentration and emission fields simultaneously by integrating multispecies and multiplatform observation data with a model. It is demonstrated that the 4D-Var and EnKF techniques showed similar quality of results for the application to meteorology (Fertig et al., 2007; Kalnay et al., 2007) and atmospheric chemistry (Skachko et al., 2016; Wu et al., 2008), when sufficient time windows are used for the 4D-Var and sufficiently frequent assimilation cycles are used for

the EnKF. 4D-Var has widely been used to optimize emission patterns of long-lived species (e.g., CO₂) consistent with all observations and with model dynamics within a long-assimilation window (Chatterjee & Michalak, 2013). In contrast, EnKF with relatively short windows is considered to be suitable for short-lived species, such as NO₂ which is main target of this study, due to the quick responses of concentrations to emissions through the fast chemistry and transport processes, given sufficient observational constraints within a short window. Meanwhile, 4D-Var requires adjoint models and its implementation for complicated systems, such as CTMs, and maintenance with various model updates and different model versions is technically challenging. The advantage of EnKF is its easy implementation for complicated systems. It does not require substantial changes in data assimilation system with changing model version and resolution. This allows us to keep updating data assimilation system using the latest version of forecast model and explore data assimilation performance at different model resolutions or different models in consistent framework (Miyazaki, Bowman, Yumimoto, et al., 2020, MOMO-Chem). Also, another important application is data assimilation coupling between meteorology and chemistry, which would benefit weather and air quality forecast (Bocquet et al., 2015). It is unrealistic to derive adjoint models which fully consider dynamical and chemical processes for coupled meteorology and chemistry data assimilation in the future.

Global chemical data assimilation frameworks for multiple trace gases have been developed using advanced data assimilation techniques and various CTMs at different horizontal resolutions from 40 to 400 km (e.g., Inness et al., 2019; Miyazaki, Sekiya, et al., 2019; Zhang et al., 2019). We investigate the hypothesis that increasing horizontal resolution of data assimilation system improves global analyses of ozone precursor emissions and concentrations of air pollutants down to a scale relevant for megacities, which were not previously investigated. In this study, three different resolutions from 2.8° typically used in global CTMs to 0.56° relevant for a megacity scale were tested for global data assimilation of multiple trace gases (ozone, NO₂, CO, HNO₃, and SO₂) from multiple sensors (OMI, GOME-2, SCIAMACHY, TES, MOPITT, and MLS) using the LETKF approach. We mainly focus on NO₂, O₃ concentrations, and NO_x emissions, because the 0.56° resolution is effective to capture the heterogeneous spatial distribution of NO₂ on a megacity scale (Sekiya et al., 2018). Our analysis provides observationally constrained and globally consistent information on emission changes at megacity scales. This overcomes the limitation of previous studies based on a widely used approach using global CTMs and bottom-up emission inventories and benefits studies on air quality and its impact on human health over different regions of the world. The remainder of this paper is structured as follows. Section 2 describes the data assimilation system and observations used for assimilation and validation. Section 3 optimizes the data assimilation settings. Section 4 evaluates the data assimilation results using assimilated and independent observations. Section 5 presents the estimated NO_x emissions, Section 6 discusses our result and its potential contribution, and Section 7 summarizes this study.

2. Data and Methods

2.1. Observation Data for Assimilation

Table 1 summarizes the assimilated satellite retrievals and the screening criteria used in this study. A super-observation approach was applied for assimilating the OMI, GOME-2, and SCIAMACHY NO₂ retrievals, and MOPITT CO retrievals (cf., Section 2.3.3). A brief description of the assimilated retrievals is given below.

2.1.1. OMI, GOME-2, and SCIAMACHY Tropospheric NO₂

Assimilated observations for tropospheric NO₂ column were obtained from the QA4ECV v1.1 L2 product for the Ozone Monitoring Instrument (OMI), the Global Ozone Experiment-2 (GOME-2), and the Scanning Imaging Absorption Spectrometer for Atmospheric Chartography (SCIAMACHY). A local equator crossing time is 13:40LT for OMI, 9:30LT for GOME-2, and 10:30LT for SCIAMACHY. The OMI tropospheric NO₂ retrieval uncertainty of a single-pixel is estimated to be typically 35%–45% over polluted regions and >100% over remote regions (Boersma et al., 2018).

2.1.2. TES Ozone

The Tropospheric Emission Spectrometer (TES) V7 L2 product was used for ozone (TES Science Team, 2017). A local equator crossing time is 13:40LT. Compared to the TES V4 products which have 5%–15% theoretical

Table 1
Observation Used for Data Assimilation

Instrument/Satellite	Variable	Data version	Pixel size	Screening criteria	References
OMI/Aura GOME-2/Metop-A SCIAMACHY/Envisat	NO ₂ TRC	QA4ECV v1.1	13 × 24 km ²	QF < 0.5	Boersma et al. (2017b)
			60 × 30 km ²	SZA > 80°	Boersma et al. (2017a)
			80 × 40 km ²	Albedo > 0.3 TropAMF /GeoAMF < 0.2	Boersma et al. (2017c)
TES/Aura	Ozone profile	Ver. 7 (Global Survey)	5–8 km	QF ≠ 1 Lat > 72°	TES Science Team (2017)
MLS/Aura	Ozone and HNO ₃ profiles	Ver. 4.2	300–400 km	$p < 215$ hPa (for ozone)	Livesey et al. (2011)
				$p < 150$ hPa (for HNO ₃)	Manney (2015)
				SF = odd QF < 1 Conv. > 1.03	Schwartz (2015)
MOPITT/Terra	CO column	Ver. 7 NIR-TIR retrievals	22 km	Lat > 65°	Ziskin (2016)
				Nighttime data	Deeter et al. (2017)
OMI/Aura	SO ₂ column	OMSO2 v3 (PBL data)	13 × 24 km ²	CRF > 0.2	Krotkov (2012)
				SZA > 50° CTP < 10 or > 50	Li et al. (2013)

Abbreviations: Conv, convergence; CRF, cloud radiance fraction; CTP, cross-track position; GeoAMF, geometric air mass factor; Lat, Latitude; p , pressure; QF, quality flag; SF, status flag; SZA, solar zenith angle; TRC, tropospheric column; TropAMF, tropospheric air mass factor.

errors over the northern mid-high latitudes (Boxe et al., 2010), the V7 products generally show improvements with respect to ozonesonde observations (Herman & Kulawik, 2013).

2.1.3. MLS Ozone and HNO₃

The Microwave Limb Sounder (MLS) v4.2 L2 products (Manney, 2015; Schwartz, 2015) were used for ozone and HNO₃. A local equator crossing time is 13:40LT. The measurement accuracy and precision were used as the observation error, which is estimated to be 30–60 ppbv and 20–200 ppbv for ozone, respectively, and 0.6 ppbv and 1.0–1.1 ppbv for HNO₃, respectively, in the lower stratosphere (Livesey et al., 2011).

2.1.4. MOPITT CO

CO column observations were obtained from the Measurement of Pollution in the Troposphere (MOPITT) V7 TIR-NIR (thermal infrared and near-infrared) multispectral L2 product (Ziskin, 2016). A local equator crossing time is 10:40LT. The overall retrieval biases, bias variability, and drift in the V7 products were improved compared to the V6 products (Deeter et al., 2017).

2.1.5. OMI SO₂

We used the OMI planetary boundary layer vertical SO₂ column L2 data produced using principal component analysis algorithm (Krotkov, 2012; Li et al., 2013). A local equator crossing time is 13:40LT. The data were excluded from the criteria as used in Fioletov et al. (2016, 2017). A fixed observation error of 0.25 DU was assumed for the OMI SO₂ assimilation, because of the lack of information on observation errors in the retrieval products.

2.2. Validation Data

2.2.1. Surface NO₂ Observations

To evaluate surface NO₂ concentrations at 0.56° resolution near large-scale sources, the surface concentrations of NO₂ were validated using surface observation network datasets of three different regions (Europe, the United States, and East Asia). For Europe, the European air quality database (AirBase) was obtained

from the European Environmental Agency (EEA, <http://www.eea.europa.eu>). For the United States, we obtained Air Quality System (AQS) network data from the United States Environmental Protection Agency (US EPA; <http://www.epa.gov/airdata>). For East Asia, the data in Hong Kong and Japan are publicly available. We used the Hong Kong Environmental Protection Department (EPD) monitoring network (<http://www.epd.gov.hk/epd>) and Japanese continuous measurement data of general air pollution at ground level from the National Institute of Environmental Studies (NIES, <http://www.nies.go.jp>). The observation sites in 38 large cities with a population of more than 1,500,000 for Europe and 2,000,000 for the United States were selected, because surface NO₂ pollution correlates with urban population in individual polluted regions (Lamsal et al., 2013). For East Asia, the validation was conducted for Hong Kong, Tokyo, Osaka, and Nagoya. In total, the validation used 83 sites for Europe, 140 sites for the United States, and 338 sites for East Asia (Hong Kong and Japan). For the comparison, we excluded urban roadside stations, and then averaged observation data at all available sites within the 0.56°-bin grid cells to minimize observation-model mismatch owing to spatial variations on the subgrid scale. Because of large spatial representativeness errors, the validation using the surface NO₂ measurements at 1.1° and 2.8° resolutions is difficult and is not discussed in this study.

Surface NO₂ concentrations were measured by commercial chemiluminescence analyzers at most of the stations (>93% of all the stations used in this study). In this method, NO₂ concentrations were derived from differences between NO with and without a molybdenum converter heated to ~400°C. Because NO₂ and other reactive nitrogen compounds are transformed into NO on the molybdenum converter, these chemiluminescence analyzers overestimate the ambient NO₂ concentrations. Thus, correction factors proposed by Lamsal et al. (2008) were applied to the data measured by the chemiluminescence method to avoid systematic overestimation. These correction factors were also used by Huijnen et al. (2010) and F. Liu et al. (2018) and were computed as follows:

$$CF = \frac{NO_2}{NO_2 + \sum ANs + 0.95 \times PAN + 0.35 \times HNO_3}, \quad (1)$$

where $\sum AN$ is the sum of all alkyl nitrate concentrations. In this study, the correction factor computed from concentrations in the data assimilation was used. The typical measurement error is 1%–5% (Gluck et al., 2003), while the correction factor should add uncertainties originating from reactive nitrogen compounds. In our approach, it is difficult to quantify the additional uncertainties from reactive nitrogen compounds.

2.2.2. Surface Ozone Observations

Surface ozone concentration analyses at resolutions of 0.56°, 1.1°, and 2.8° were evaluated at rural and remote locations using four regional and global monitoring networks excluding urban observations to avoid large spatial representativeness errors. For Europe, European Monitoring and Evaluation Program (EMEP) data were obtained from NILU EBAS (<http://ebas.nilu.no>). For the United States, Clean Air Status and Trends Network (CASTNET) data obtained from the United States EPA (<https://www.epa.gov/castnet>) were used. For East Asia, Acid Deposition Monitoring Network in East Asia (EANET) data (<http://www.eanet.asia>) were collected. For the rest of the world, Global Atmosphere Watch (GAW) data were obtained from World Data Center for Greenhouse Gases (WDCGG, <https://gaw.kishou.go.jp/>). For the comparison, simulated and analyzed ozone concentrations were linearly interpolated to the observation locations from their four surrounding grids. We used all available data in sites at altitudes lower than 1,500 m for evaluation of surface air pollution in the planetary boundary layer (118 sites for Europe, 70 sites for the United States, 11 sites for East Asia, and 21 sites for other regions).

2.2.3. Arctic Aircraft Campaign Observations

Vertical profiles of ozone, NO₂, HNO₃, PAN, OH, and HO₂ were obtained from NASA's 2008 Arctic research on the composition of the troposphere from aircraft and satellites (ARCTAS) B campaign (Jacob et al., 2010). The ARCTAS-B campaign was conducted using NASA's DC-8 aircraft from June 18 to July 14. The DC-8 flight tracks covered regions between 50°N and 70°N during ARCTAS-B. NO₂ and ozone were measured via chemiluminescence (Weinheimer et al., 1994), while HNO₃, PAN, OH, and HO₂ were analyzed using chemical ionization mass spectrometry (Cantrell et al., 2003; Crounse et al., 2006; Kim et al., 2007).

We used merged data for 1-min duration obtained from NASA LaRC Airborne Science Data for Atmospheric Composition (<http://www-air.larc.nasa.gov>). For the comparison, we sampled simulated profiles at the model time closest to the measurement using 2-h model outputs, and used spatial linear interpolation to the aircraft locations from the four surrounding grid cells. The observed and simulated profiles were compared by averaging the data within 14 vertical pressure bins from 950 to 100 hPa.

2.2.4. Ozone Sonde Observations

The observed vertical profiles of ozone were obtained from the World Ozone and Ultraviolet Data Center (WOUDC; <http://www.woudc.org>), Southern Hemisphere Additional Ozone sondes (SHADOZ; Sterling et al., 2018; Thompson et al., 2017; Witte et al., 2017, 2018), and the NOAA Earth System Research Laboratory (ESRL) Global Monitoring Division (GMD; <ftp://ftp.cmdl.noaa.gov/ozwv/ozone>). We selected ozone-sonde stations with more than nine profiles for North America and two profiles for other regions during June 29–July 21, 2008. The period partly covered the ArcIONS campaign in the United States (<https://tropo.gsfc.nasa.gov/arcions>). We used 24 profiles at 6 stations for the northern high latitudes (55°N–90°N), 104 profiles at 8 stations for North America (20°N–55°N), 39 profiles at 7 stations for Europe (20°N–55°N), 18 profiles at 4 stations for East Asia (20°N–55°N), 26 profiles at 10 stations for the tropics (20°S–20°N), and 31 profiles at 10 stations for the southern mid-high latitudes (90°S–20°S). The observed and simulated ozone profiles were compared at ozone-sonde locations in the same vertical pressure bin as used in the comparison with the ARCTAS-B aircraft observation.

2.3. Data Assimilation Approach

2.3.1. CHASER Global Chemical Transport Model

The forecast model used in the data assimilation system is CHASER V4.0 (Sekiya et al., 2018; Sudo et al., 2002; Watanabe et al., 2011) to obtain globally consistent a priori information on concentration fields which is necessary to make the best use of global satellite observations of atmospheric trace gases. We employed a horizontal resolution of T42 (i.e., 2.8°), T106 (i.e., 1.1°), and T213 (i.e., 0.56°). The 32 vertical layers from the surface to ~40 km were commonly used at the three horizontal resolutions. The vertical resolution was finer than 1 km per layer in the troposphere and lower stratosphere and increased to 3.5 km per layer from the middle stratosphere. CHASER simulates spatial and temporal variations in chemical species (ozone, HO_x, H₂O₂, NO_x, N₂O₅, HNO₃, PAN, CO, C₂H₆, C₂H₄, C₃H₈, C₃H₆, C₅H₈, C₁₀H₁₆, CH₃COCH₃, HCHO, CH₃CHO, CH₃OH, SO₂, SO₄, DMS, NH₃, NH₄, and other 63 species) in the troposphere and stratosphere, by calculating tracer transport (advection, cumulus convection, and vertical diffusion), emissions, dry and wet deposition, and chemical processes (262 reactions) including the ozone–HO_x–NO_x–CH₄–CO system with nonmethane volatile organic compounds oxidation. Stratospheric chemistry (i.e., halogen chemistry) was adapted from the CCSR/NIES CCM. Additionally, a synthetic ozone tracer of stratospheric origin was calculated in the troposphere.

The meteorological fields were calculated “on-line” by dynamical and physical components of the CHASER V4.0, which is equivalent to the MIROC-AGCM atmospheric general circulation model (K-1 Model Developers, 2004), while interactions between atmospheric constituents and climate were not considered to keep the same meteorological fields among all the ensemble members. The calculated meteorological fields were used in the chemistry module at every time step (i.e., 1–4 min at 0.56°, 2–8 min at 1.1°, and 5–20 min at 2.8° resolution). To reproduce past meteorological fields and calculate short-term variability, the simulated temperature and horizontal wind fields were nudged to the 6-h ERA-Interim reanalysis data (Dee et al., 2011) with a relaxation time of 5 days for temperature and 0.7 days for horizontal winds. The reanalysis data (at a resolution of 0.75°) were linearly interpolated to each model grid and then used in the nudging. We used an optimized setting for the cumulus convection parameterization (prognostic Arakawa-Schubert scheme; Emori et al., 2001) at each resolution based on sensitivity calculations (Sekiya et al., 2018).

The a priori surface NO_x, CO, and SO₂ emissions were obtained from bottom-up emission inventories. Anthropogenic emissions were taken from the HTAP_v2.2 (Janssens-Maenhout et al., 2015) for 2008. Monthly mean biomass burning emissions for 2008 were taken from the Global Fire Emissions Database (GFED) version 4.1s (Randerson et al., 2018). Soil emissions were obtained from the Global Emissions Initiative (GEIA) database (Yienger & Levy, 1995). We also applied a diurnal cycle scheme for surface NO_x emissions,

as developed by Miyazaki, Eskes, and Sudo (2012), in which different diurnal cycles are applied depending on the dominant emission category, that is, anthropogenic, biomass burning, or soil emissions, for each region. The a priori lightning NO_x source was calculated as a function of cloud top height in the cumulus convection parameterization in the models at each model time step, following Price and Rind (1992). The annual lightning NO_x sources in the model simulations were estimated to be 5.5 Tg N yr^{-1} at 0.56° , 5.6 Tg N yr^{-1} at 1.1° , and 5.4 Tg N yr^{-1} at 2.8° resolution for 2008 (Sekiya et al., 2018).

2.3.2. Ensemble Kalman Filter Data Assimilation

We used the multiconstituent data assimilation system (Miyazaki, Sekiya, et al., 2019). The data assimilation technique employed is LETKF (Hunt et al., 2007), because LETKF can easily be applied to complicated tropospheric chemistry system and flow-dependent error covariance matrix can be obtained from an ensemble model forecast. The LETKF-based multiconstituent data assimilation system has been developed by Miyazaki, Eskes, Sudo, et al. (2012) and extended to the estimation of lightning NO_x sources (Miyazaki et al., 2014) and diurnal variations in surface NO_x emissions (Miyazaki et al., 2017). To perform chemical data assimilation at a high resolution, we optimized the vectorization of the data assimilation code which increased the computational file input/output efficiency. This is now 4.6 times faster than before without the optimization for our supercomputer system, which enabled us to long-term and 0.56° -resolution data assimilation calculations.

In the data assimilation, the background error covariance is estimated from background ensemble perturbations, assuming that ensemble model forecasts capture the structure of the background error covariance. In the forecast step, the background ensemble mean, $\bar{\mathbf{x}}^b$, and its perturbation, \mathbf{X}^b , are obtained from each member of ensemble forecasts at every model grid.

$$\bar{\mathbf{x}}^b = \frac{1}{k} \sum_{i=1}^k \mathbf{x}_i^b; \quad \mathbf{X}_i^b = \mathbf{x}_i^b - \bar{\mathbf{x}}^b, \quad (2)$$

where \mathbf{X}_i^b is the i th column of an $N \times k$ matrix \mathbf{X}^b , N signifies the system dimension (i.e., the state vector size \times the physical system dimension), and k is the ensemble size. The background error covariance \mathbf{P}^b is thus obtained with the following equation:

$$\mathbf{P}^b = \mathbf{X}^b (\mathbf{X}^b)^T. \quad (3)$$

The background error covariance varies with time and space, which reflects the physical and chemical processes at observation locations.

In the analysis step, an ensemble of background vectors and an ensemble of background perturbations in the observation space are obtained by applying the observation operator H . The analysis ensemble mean is obtained by updating the background ensemble mean, as follows:

$$\bar{\mathbf{x}}^a = \bar{\mathbf{x}}^b + \mathbf{X}^b \tilde{\mathbf{P}}^a \left(H(\mathbf{x}_i^b) - \overline{H(\mathbf{x}_i^b)} \right)^T \mathbf{R}^{-1} \left(\mathbf{y}^o - \overline{H(\mathbf{x}_i^b)} \right), \quad (4)$$

where \mathbf{y}^o is the observation vector, \mathbf{R} represents the $p \times p$ observation error covariance, p indicates the number of observations, and $\tilde{\mathbf{P}}^a$ is the $k \times k$ local analysis error covariance in the ensemble space. The observation error covariance is provided for each retrieval. The local analysis error covariance is estimated as

$$\tilde{\mathbf{P}}^a = \left[\frac{(k-1)\mathbf{I}}{1+\Delta} + \left(H(\mathbf{x}_i^b) - \overline{H(\mathbf{x}_i^b)} \right)^T \mathbf{R}^{-1} \left(H(\mathbf{x}_i^b) - \overline{H(\mathbf{x}_i^b)} \right) \right]^{-1}, \quad (5)$$

where Δ is a covariance inflation factor ($=8\%$ per analysis cycle for stratospheric ozone and HNO_3 and 7% per analysis cycle for other species). The covariance inflation was applied at every analysis step to prevent the underestimation of the background error covariance and resultant filter divergence caused by model and sampling errors. The analysis perturbations \mathbf{X}^a in the model space is obtained by transforming the background ensemble perturbations \mathbf{X}^b , as follows:

$$\mathbf{X}^a = \mathbf{X}^b \left[(k-1) \tilde{\mathbf{P}}^a \right]^{1/2}. \quad (6)$$

The new ensemble members x_i^b for the next step are obtained from the ensemble model forecast starting from the analysis ensemble x_i^a .

The state vector includes surface emissions of NO_x, CO, and SO₂, the lightning NO_x production rate, and the concentrations of 35 chemical species for every grid point. To improve filter performance, the covariance among nonrelated or weakly related variables was set to zero, following Miyazaki, Eskes, Sudo, et al. (2012). Surface NO_x, CO, and SO₂ emissions and lightning NO_x sources are estimated based on a state argumentation method (e.g., Evensen, 2009) as performed in our previous studies (Miyazaki et al., 2017; Miyazaki, Sekiya, et al., 2019). In this approach, emissions are estimated using the relationships between the observed variable and the corresponding emissions in background error covariance which is produced by ensemble CTM forecasts. For NO_x emissions, emission factors are optimized at resolutions of 2.8° and 1.1° as done by Miyazaki et al. (2017) and Miyazaki, Sekiya, et al. (2019), whereas emission fluxes are directly optimized at 0.56° resolution. The two approaches provide slightly different a-posteriori emissions because of boarder Gaussian error distributions assumed in the emission flux optimization approach than those in the emission factor optimization approach (cf., Section 3.2). Diurnal cycles of surface NO_x emissions were optimized by assimilating the multiple instruments observed at different local times (i.e., OMI, GOME-2, and SCIAMACHY retrievals in this study) using the method developed by Miyazaki et al. (2017). Cloudy-scene NO₂ retrievals were separately used for optimizing lightning NO_x sources, following the methods proposed in Miyazaki et al. (2014). The optimized SO₂ emissions are not discussed in this study and will be investigated in a separate study.

The initial a priori error was set as 40% for surface NO_x and CO emissions, and 60% for the lightning NO_x source. We also applied a covariance inflation to the emission sources during the analysis step to prevent covariance underestimation. This covariance inflation is important to maintain realistic uncertainties in the emission estimates (Miyazaki et al., 2015). In this study, the standard deviation was artificially inflated to a predefined minimum value obtained through sensitivity calculations (i.e., 68% and 48% of the a priori surface NO_x and CO emissions, respectively). These predefined minimum values were used at all resolutions.

2.3.3. Super-Observation Approach

A super-observation approach was employed to generate observation data representative of the area of the model grid cells. Boersma et al. (2016) discussed strategies for comparing satellite retrievals and model simulations. Their results advocated that a super-observation approach would be better than thinning out satellite retrievals to one per grid cell, which minimize spatial representativeness errors. The super-observation errors were limited to 5%–10% with a fractional coverage of more than 0.5 at 3 × 2 model resolution and became larger at 0.5° resolution, because a lack of pixels near strong local sources produces larger horizontally spatial representativeness errors at high-resolution grids than at low-resolution grids.

In our approach, we applied a super-observation technique to tropospheric NO₂ column, total CO column, and total SO₂ column measurements, while not applying to ozone and HNO₃ profiles, as in Miyazaki, Eskes, and Sudo (2012), Miyazaki et al. (2015), and Miyazaki, Sekiya, et al. (2019). The super-observation grid resolutions were identical to those of the model grid cells. The mean concentration of all data within a super-observation grid cell was generated as follows:

$$\bar{y} = \left(\sum_{l=1}^m w_l y_l \right) / \left(\sum_{l=1}^m w_l \right), \quad (7)$$

where \bar{y} is the mean concentration, y_l represents the concentration of individual data, w_l signifies the weighting factor for individual data defined as the coverage area of each data pixel within a super-observation grid cell, and m is the number of observations within a super-observation grid cell. We applied the same weighting factor for averaging kernel.

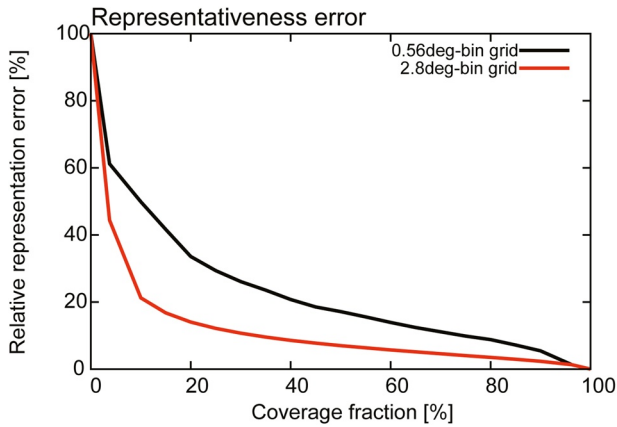


Figure 1. Relative representativeness error (%) for OMI as a function of coverage fraction at 2.8°- and 0.56°-bin grids over 60°S–60°N using QA4ECV retrievals in 2008.

The spatial representativeness error was applied when data coverage is incomplete. The observation error for the super-observation σ_{super} was calculated as a combination of measurement error $\sigma_{\text{super, mean}}$ and spatial representativeness error $\sigma_{\text{super, rep}}$:

$$\sigma_{\text{super}} = \sqrt{\sigma_{\text{super, mean}}^2 + \sigma_{\text{super, rep}}^2}. \quad (8)$$

The measurement error for the super-observation was formulated as in Eskes et al. (2003):

$$\sigma_{\text{super, mean}} = \left(\left(\sum_{l=1}^m w_l \sigma_l \right) / \left(\sum_{l=1}^m w_l \right) \right) \sqrt{\frac{1-c}{m} + c}, \quad (9)$$

where σ_l is the retrieval error of individual data, and c represents the error correlation among data. Although the exact value of the error correlation is barely known, we employ a 15% error correlation, as in Miyazaki, Eskes, and Sudo (2012).

The spatial representativeness error was computed using a relative representativeness error as a function of coverage fraction (α , $0 < \alpha < 1$), $f_{\text{rep}}(\alpha)$, and the mean concentration \bar{y} :

$$\sigma_{\text{super, rep}} = f_{\text{rep}}(\alpha) \times \bar{y}. \quad (10)$$

The relative representativeness error was estimated by the following procedure: (1) randomly reducing the number of pixels m in Equation 7 first by 1, then by 2, and so on, until $m - 1$; (2) generating new estimates \bar{y}' ; (3) repeating 100 times; and (4) computing the relative root-mean-squared difference from the original mean concentration \bar{y} . We applied this procedure to the grid cells with $\alpha > 0.9$ and $\bar{y} > 0.5 \times 10^{15}$ molecules cm^{-2} .

The relative spatial representativeness error (Figure 1) was estimated at 2.8 and 0.56° resolutions using the OMI retrievals in 2008 over 60°S–60°N. The relative representativeness errors decreased as the data coverage fraction increased as expected, with a steep decrease for coverage of less than 10% (e.g., >60% at 4% coverage at 0.56° resolution). The relative representativeness error was larger by a factor of 2.4–2.8 at a coverage fraction of 10%–90% using a 0.56°-bin grid than that using a 2.8°-bin grid, which might suggest smaller analysis increments at 0.56° resolution. However, the average coverage fraction is higher by a factor of two at 0.56° resolution than at 2.8° resolution, which might suggest that observation data with smaller representativeness error are incorporated into the system more efficiently by data assimilation at 0.56° resolution and then propagated in space and time. The impact of using the super-observation approach will be evaluated in Section 3.1.

2.4. Experimental Settings

We performed three types of assimilation runs which simultaneously optimized concentration and emission fields (Table 2). (1) Sensitivity data assimilation calculations were performed to optimize the assimilation settings at 0.56° resolution for April 23–May 3, 2008 (Experiment nos. 1–9). (2) Two 30-day data assimilation calculations were conducted at 0.56° resolution with the optimized assimilation setting during boreal spring and summer of 2008 (Nos. 10–11). These calculations were used to evaluate the data assimilation performance for different seasons (Sections 4.1, 4.2 and 5.1). (3) Multiresolution 30-day data assimilation calculations were conducted at 0.56°, 1.1°, and 2.8° resolutions for boreal summer of 2008 (Nos. 12–14) to elucidate the impacts of changing horizontal model resolution at same ensemble size (i.e., 32) (Sections 4.3 and 5.2). The data assimilation at 1.1° resolution was identical to Tropospheric Chemistry Reanalysis version 2 (TCR-2, Miyazaki, Bowman, et al., 2019; Miyazaki, Bowman, Sekiya, et al., 2020). All the data assimilation runs optimized concentration and emission fields simultaneously. The a priori emissions and assimilated retrievals were common among the experiments. Because of the distinct diurnal cycles of

Table 2
List of the Data Assimilation and Model Simulation Calculations Performed in This Study

No.	Period	Horizontal resolution	Ensemble size	Note
1	April 23–May 3	0.56°	64	OMI NO ₂ DA with super-observation approach and with emission flux optimization
2				OMI NO ₂ DA without super-observation approach and with emission flux optimization
3				OMI NO ₂ DA with super-observation approach and with emission factor optimization
4	April 23–May 3	0.56°	64	Multi-constituent DA
5			32	Multi-constituent DA
6			96	Multi-constituent DA
7			64	Multi-constituent DA with L of 262 km for NO ₂
8			64	Multi-constituent DA with L of 736 km for NO ₂
9			64	Multi-constituent DA with L of 1971 km for NO ₂
10	April 1–30	0.56°	64	Multi-constituent DA
11	June 22–July 21			
12	June 22–July 21	0.56°	32	Multi-constituent DA
13		1.1°		
14		2.8°		
15	January 1–July 21	0.56°	N/A	Model simulation
16		1.1°		
17		2.8°		

Note. Multi-constituent DA indicates the data assimilation using all the satellite observations listed in Table 1. DA and L are data assimilation and localization length, respectively. The optimized data assimilation settings described in Section 3 were used unless stated otherwise.

the tropospheric chemistry system, the data assimilation cycle was set to be short (i.e., 120 min). The model simulation without any data assimilation and using the a priori emissions were also performed for the same periods (Nos. 15–17).

2.5. Statistical Significance Test

Significance levels of differences in mean concentrations and root-mean-square (RMS) innovations and errors between with and without data assimilation, different assimilation parameters, and different horizontal resolutions were determined using two-sample *t*-test, which is based on the assumption that a population of data follows Gaussian distribution. The population of chemical concentrations is likely to follow log-normal distribution, which approximately follows Gaussian distribution after logarithmic transformation. The *t*-value was calculated after logarithmic transformation as

$$t = \frac{\bar{x}_1 - \bar{x}_2}{\sqrt{\frac{s_1^2}{N_1} + \frac{s_2^2}{N_2}}}, \quad (11)$$

where \bar{x} is mean value of logarithm of target variable, s is standard deviation of logarithm of target variable, and N is the number of data. The mean value and its standard deviation are calculated using values obtained from each ensemble member when we compared the sensitivity data assimilation runs (Section 3). For the comparison between the model simulation and data assimilation, we calculated temporal mean and variance at each grid and determine the level of significance for mean difference using two-sample *t*-test, because the model simulation does not provide any error information regarding ensemble spread

(Sections 4 and 5). Temporal variance is used for a statistical significance when the simulated mean fields in two different simulations are compared (e.g., Banerjee et al., 2016; Meul et al., 2018).

For RMS innovations and errors, the *t*-test and Mann-Whitney *U*-test were used to determine the level of significance, because the RMS innovations and errors may not be normally distributed. The *U*-statistics were calculated as

$$U = \min(U_1, U_2), \quad (12)$$

$$U_1 = N_1 N_2 + \frac{N_1(N_1 + 1)}{2} - R_1, \quad (13)$$

$$U_2 = N_1 N_2 + \frac{N_2(N_2 + 1)}{2} - R_2, \quad (14)$$

where *N* is the number of data, *R* is the sum of ranks in samples.

Significance of differences in correlation coefficients in two samples were tested by calculating the *Z* value using Fisher's *z*-transformation as follows,

$$Z = \frac{z'_1 - z'_2}{\sqrt{\frac{1}{N_1 - 3} + \frac{1}{N_2 - 3}}}, \quad (15)$$

$$z' = \frac{1}{2} \ln \frac{1 + r}{1 - r}, \quad (16)$$

where *z'* is the Fisher's *z*-transformation, *N* is the number of data, and *r* is the correlation coefficient.

3. Optimization of the Data Assimilation System

3.1. Super-Observation Approach

To assess the impact of the super-observation approach, we performed data assimilation calculations using the OMI NO₂ all individual retrievals and super-observations. As summarized in Table 3, the global Pearson's correlation coefficient calculated from each super-observation and analysis and RMS innovation with and without the application of the super-observation approach were comparable at 0.56° resolution, while the RMS innovation was improved by up to a few percent over major polluted regions. The spatial and temporal variations in analysis increments became slightly smoother using super-observation approach (i.e., the standard deviation of analysis increments was smaller by up to 1.5% over polluted regions). In general, the impact of the super-observation is larger at coarser resolution (e.g., 2.8° resolution, not shown), because 0.56° resolution (~60 km) is closer to the pixel size of OMI retrievals (13 × 24 km²). Nevertheless, the number of assimilated observations was reduced by a factor of ~10 using super-observation approach at 0.56° resolution compared to those in individual OMI observations without super-observations. The reduced number of assimilated measurements resulted in about 10% reductions in the total computational cost of data assimilation. With higher resolution (<7 km) measurements such as TROPOMI and geostationary satellites, the super-observation approach would be even more important at 0.56° resolution.

The performance of OMI NO₂ data assimilation with super-observation approach was confirmed by the χ^2 test (Ménard & Chang, 2000; Zupanski & Zupanski, 2006). χ^2 value is diagnosed from the ratio of the OmF (i.e., $y^o - H(x^b)$) to estimated error covariance in the observational space ($HP^bH^T + R$) as

$$Y = \frac{1}{\sqrt{N}} (HP^bH^T + R)^{-1/2} (y^o - H(x^b)) \quad (17)$$

$$\chi^2 = \text{trace} YY^T. \quad (18)$$

Table 3
Correlation Coefficients and Root Mean Square (RMS) Innovations of Observation-Minus-Forecast (OmF) for Tropospheric NO₂ Column Derived From OMI During April 29 to May 3, 2008

No.	Descriptions of sensitivity calculation	Correlation	RMS innovation
1	Assimilation of OMI with super-observation and with emission flux optimization	0.85	0.42 ± 0.07
2	Assimilation of OMI without super-observation and with emission flux optimization	0.85	0.42 ± 0.07
3	Assimilation of OMI with super-observation and with emission factor optimization	0.82*	0.51 ± 0.11* ^a
4	Standard setting ($N = 64$, $L = 1,369$)	0.85	0.41 ± 0.08
5	Smaller ensemble size ($N = 32$, $L = 1,369$)	0.83*	0.46 ± 0.06* ^a
6	Larger ensemble size ($N = 96$, $L = 1,369$)	0.86*	0.40 ± 0.09 ^a
7	Shorter cutoff length ($N = 64$, $L = 273$)	0.87*	0.40 ± 0.10
8	Shorter cutoff length ($N = 64$, $L = 766$)	0.86*	0.40 ± 0.10
9	Longer cutoff length ($N = 64$, $L = 1,971$)	0.83*	0.45 ± 0.06* ^a

Note. The correlation coefficient and RMS innovation with standard deviation among ensemble members were obtained from the calculations over 6 days after a spin-up. The unit of RMS innovations is 1,015 molecules cm². The numbers of first column are common in Tables 2 and 3. N and L denote ensemble size and cutoff length (km), respectively. The asterisk and “a” indicate that mean difference from the standard settings (No. 1 for No. 2 and 3, and No. 4 for No. 5 to 9) is statistically significant at the 95% confidence level using the two-sample t -test and Mann-Whitney U -test, respectively. The ranges of RMS innovations are standard deviation calculated from each ensemble member.

The mean value of χ^2 over 60°S–60°N during April 29–May 3 was 1.02, which was comparable to the ideal χ^2 value of 1. Over regions with $> 0.5 \times 10^{15}$ molecules cm^{−2} of the tropospheric NO₂ column, the mean χ^2 value was 1.37. These results confirmed that the data assimilation system underestimated the estimated error covariance over polluted regions, whereas the estimated error covariance was underestimated over remote regions, partly because simple multiplicative inflation technique was used in this study. Spatially and temporally varying inflation factors using adaptive multiplicative inflation technique (Anderson, 2009; Miyoshi, 2011) would help improve these biases of the estimated error covariance.

3.2. Emission Optimization Approach

To determine the emission optimization approach, the data assimilation with emission flux and factor optimization approaches were performed at 0.56° resolution. As summarized in Table 3, the optimization of emission flux was characterized by better agreements with the assimilated observations compared to the optimization of emission factor (by 20% for RMS innovation which was statistically significant at the 95% confidence levels using two-sample t -test and Mann-Whitney U -test); this can be associated with broader emission error distributions in the optimization of emission flux, particularly over polluted regions.

3.3. Data Assimilation Parameters

The optimal data assimilation setting can vary with model resolution. The degrees of freedom of the system increase with horizontal resolution, while model errors evolve differently between models at different resolutions. Table 3 summarizes the evaluation results of the sensitivity data assimilation runs after a spin-up against the tropospheric NO₂ from OMI and tropospheric ozone from TES, respectively. For tropospheric NO₂ (Table 3), increasing the ensemble size from 32 to 64 improved the correlation coefficient between each super-observation and analysis from 0.83 to 0.85 with significance at the 99% confidence and reduced the RMS innovation by 11% with statistical significance at the 95% confidence using the t -test and U -test, whereas improvements were much smaller when the ensemble size was increased from 64 to 96. Increasing the ensemble size from 32 to 64 slightly reduced the regional NO_x emissions over China (by up to 6%). Using the same ensemble size (64), the RMS innovation was 10% larger in the assimilation with a cutoff radius of 1,971 km than the other cutoff radii, with small differences (<3%) for assimilation runs using cutoff radii of

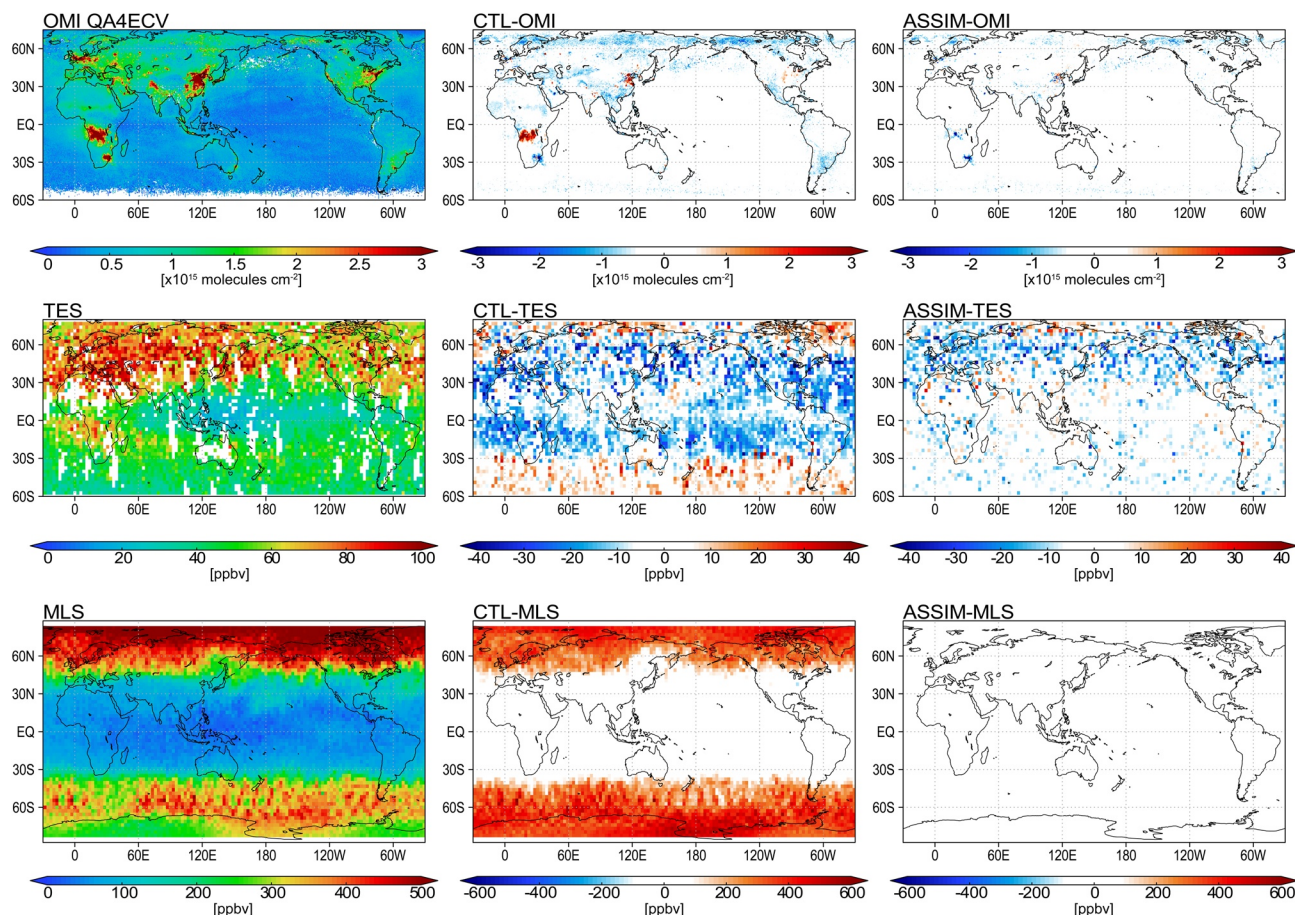


Figure 2. Global distributions of tropospheric NO_2 column ($\times 10^{15}$ molecules cm^{-2} ; upper row), ozone at 500 hPa (ppbv; middle row), and ozone at 215 hPa (ppbv; lower row) derived from OMI, TES, and MLS, respectively (left column), and differences between the model simulation and satellite retrievals (middle column) and between the data assimilation and satellite retrievals (right column) during June 29 to July 21, 2008. Tropospheric NO_2 and ozone fields are mapped onto 0.56° - and 2.8° -bin grids for visibility, respectively.

273, 766, and 1,369 km, with statistical significance at the 95% confidence level using the *t*-test and *U*-test. Nevertheless, the differences in RMS innovation and correlation coefficients between experiments at ensemble sizes of 32 and 64 and between experiments with standard and longer cutoff length were statistically significant. The improvements in the experiment at ensemble size of 96 were small relative to that at ensemble size of 64, considering required computational resources. Thus, we employed an ensemble size of 64 and cutoff radii of 1,369 km for NO_x emission as the optimal setting for the system based on the obtained results.

4. Evaluation of Concentration Analyses Derived From Data Assimilation

4.1. Consistency With Assimilated Measurements

Using the optimized data assimilation setting, we evaluated data assimilation performance at 0.56° resolution. Figure 2 and Table 4 show comparison results against the assimilated measurements for the boreal spring and summer of 2008. The agreement levels were similar between the boreal spring and summer of 2008. For the boreal summer, data assimilation reduced the global mean biases and RMSE of the tropospheric NO_2 column by 72%–94% and 17%–41%, respectively, against OMI, GOME-2, and SCIAMACHY, whereas it increased the global spatial Pearson's correlation coefficients between the observed and simulated mean concentration fields by 0.04–0.07. Over major polluted regions, the RMSEs with respect to OMI were reduced by 15% over Europe, 28% over the United States, and 38% over China. The RMSEs were also reduced by 45% in average over regions where soil NO_x emissions are dominant ($>50\%$). The negative model bias against TES ozone over the tropics and the northern midlatitudes (20°S – 55°N) at 500 hPa was reduced

Table 4

Mean Bias (MB), Spatial Correlation Coefficient (S-Corr.), and Root Mean Square Error (RMSE) for Mean Concentration Fields of Tropospheric NO₂ Column Compared With OMI, GOME-2, and SCIAMACHY, Ozone at 500 hPa Compared With TES, and Ozone at 215 hPa Compared With MLS in the Data Assimilation and Model Simulation (in Brackets) During 2008 Boreal Spring (April 8–30) and Summer (June 29–July 21)

Observation	Boreal spring (April 8–30, 2008)			Boreal summer (June 29–July 21, 2008)		
	MB	S-Corr.	RMSE	MB	S-Corr.	RMSE
OMI NO ₂	−0.06 (−0.21)	0.94 (0.87)	0.24 (0.40)	−0.06 (−0.22)	0.92 (0.85)	0.23 (0.39)
GOME-2 NO ₂	−0.05 (−0.22)	0.92 (0.84)	0.32 (0.51)	−0.04 (−0.21)	0.91 (0.85)	0.28 (0.43)
SCIAMACHY NO ₂	−0.03 (−0.21)	0.86 (0.81)	0.56 (0.67)	0.01 (−0.17)	0.85 (0.81)	0.38 (0.46)
TES ozone (500 hPa)	−4.44 (−12.47)	0.88 (0.71)	9.32 (17.64)	−2.65 (−8.45)	0.88 (0.67)	8.41 (15.39)
MLS ozone (215 hPa)	−19.85 (72.77)	0.98 (0.94)	49.85 (160.10)	−8.4 (95.76)	0.99 (0.94)	26.34 (198.23)
MLS HNO ₃ (147 hPa)	−0.06 (0.09)	0.96 (0.92)	0.46 (0.70)	0.04 (0.29)	0.92 (0.90)	0.48 (0.79)

All statistics were calculated at 0.56°-bin grid. The units of MB and RMSE are $\times 10^{15}$ molecules cm^{−2} for OMI, GOME-2, and SCIAMACHY NO₂ and ppbv for TES Ozone, MLS Ozone and HNO₃.

by 69%, while the positive model bias over the southern midlatitudes (20°S–55°S) was reduced by 44%. Large positive model biases against MLS ozone at 215 hPa were mostly removed in the extratropics, whereas the negative model bias in the tropical upper troposphere was reduced by 43%. Positive model biases against MLS HNO₃ at 147 hPa were reduced by 82% over the extratropics of both hemispheres (20°–90°N and °S) and by 53% over the tropics (20°S–20°N). The obtained analysis errors were mostly comparable to the uncertainties of the assimilated measurements. The improved agreements confirm that the measurements were successfully assimilated into the system for the entire globe.

4.2. Performance of Data Assimilation at 0.56° Resolution

4.2.1. Validation Using Surface NO₂ Measurements

Figure 3 and Table 5 compare surface NO₂ concentrations against the in situ monitoring networks in Europe, the United States, and East Asia (Hong Kong and Japan). The model biases were positive over these regions. By data assimilation, in Europe, the positive mean bias was reduced by 72%, with large bias reduction by 97% in northern Europe (46°N–60°N). In the United States, the positive model bias was reduced by 94%. The regional bias reduction was larger over the eastern United States (by 87%) than over the western United States (by 67%). In East Asia, the positive mean bias was reduced by 81%. The RMSEs were also reduced by 33%, 67%, and 75% in Europe, the United States, and East Asia, respectively. These differences in mean biases and RMSEs were statistically significant at the 99% confidence level using the *t*-test for mean biases and RMSEs and the *U*-test for RMSEs.

Table 6 summarizes the validation results in the selected nine cities in Europe, eight cities in the United States, and two cities in East Asia. For Europe, a city that is the most populated in each country was selected. For the United States, we selected two cities that were the most and second most populated, respectively, in the northeast, southeast, midwest, and western United States. Hong Kong and Tokyo were selected in East Asia. In most of the selected cities, the model biases were reduced by data assimilation, with large bias reductions by more than 95% in Detroit, Philadelphia, and Tokyo. Over most large urban areas in Europe, the bias reductions were more than 50%. As an exception, over Rome, Madrid, and Lisbon, the small improvements (<50%) could be attributed to large spatial representativeness errors between in situ measurements and analyses, because the areas of these three cities are smaller than a model grid cell ($\sim 3,600$ km²). Overall validation results suggest that the data assimilation at 0.56° resolution is effective for improving surface NO₂ concentrations in large urban areas.

The diurnal cycles for surface NO₂ with a minimum during mid-day were commonly observed in Europe, the United States, and East Asia (Figure 3), which reflects chemical NO₂ loss with OH, photodissociation of NO₂, diurnal variability in NO_x emissions, and diurnal cycles of boundary layer height. In the selected cities, the model overestimation in the mean NO₂ diurnal amplitude was reduced by $49 \pm 51\%$, $69 \pm 41\%$,

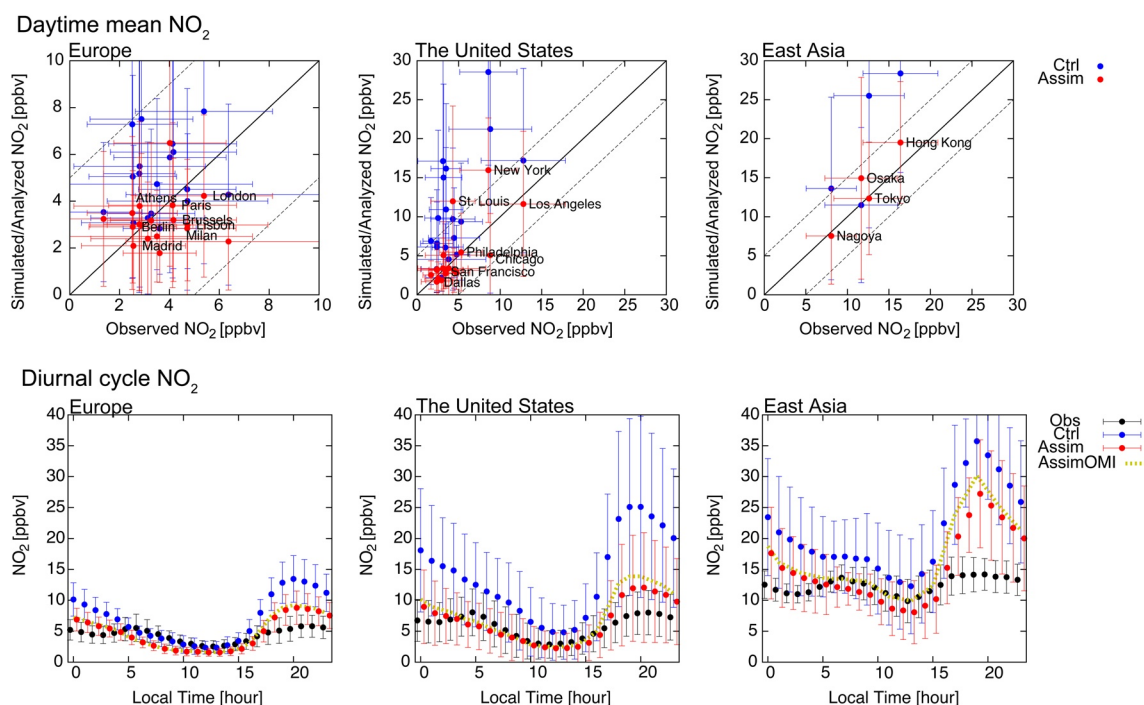


Figure 3. Scatter plots (upper row) and mean diurnal cycles (lower row) of surface NO_2 concentrations (ppbv) derived from in situ measurements, model simulation, and data assimilation at large cities in Europe (left column), the United States (middle column), and East Asia (right column) during June 29 to July 21, 2008. The black, red, blue, and yellow symbols are results from the in situ measurements, the data assimilation, the control model simulation, and the data assimilation without GOME-2 and SCIAMACHY. The error bars are standard deviation of NO_2 time series.

and $22 \pm 78\%$ in Europe, the United States, and East Asia, respectively, by data assimilation, while the differences in amplitudes over Europe and the United States were statistically significant at the 95% confidence level using the t -test. The NO_2 ratio between morning and early afternoon after data assimilation better agreed with in situ measurements in four of the nine cities in Europe, and five of the eight cities in the United States. These improvements corresponded to reduced diurnal emission amplitude by 45%, 58%, and 19% in Europe, the United States, and East Asia, respectively (figure not shown), through the assimilation of the multiple NO_2 retrievals obtained at different overpass times and its application to diurnal emission variability (cf., Section 2.1). By assimilating GOME-2 and SCIAMACHY NO_2 retrievals in addition to OMI NO_2 , the amplitudes of NO_x emission diurnal cycles were reduced by 3%–7% in the large urban areas, which led to 3%–8% reductions in the amplitude of surface NO_2 concentrations. Corrections made to OH and NO_2/NO partitioning were also important. The multiconstituent data assimilation reduced the diurnal amplitude of OH concentrations by 7% and 27% in Europe and the United States, respectively, and increased it by 29% in East Asia. The diurnal amplitude of NO_2/NO_x ratio was slightly reduced by less than 10% over these three regions. We confirmed that more than 55% of the corrections made to OH and NO_2/NO partitioning were

Table 5

Slope, Intercept, Mean Bias (MB), Correlation Coefficient (Corr.), and Root Mean Square Error (RMSE) for Daytime (8–20LT) Surface Concentration of NO_2 Obtained From the Data Assimilation and Model Simulation (in Brackets) Compared to In Situ Measurement Networks in Large Urban Areas Over Europe, the United States, and East Asia (Hong Kong and Japan)

Region	Slope	Intercept	MB	Corr.	RMSE
Europe	0.86 ± 0.36 (1.29 ± 0.52)	0.11 ± 1.34 (0.39 ± 1.93)	-0.40 ± 0.77 (1.45 ± 0.96)	0.08 (0.15)	1.54 ± 0.67 (2.29 ± 1.59)
The United States	1.42 ± 0.57 (2.46 ± 1.10)	-1.46 ± 2.59 (-0.16 ± 5.02)	0.39 ± 0.78 (6.29 ± 0.88)	0.71 (0.64)	2.75 ± 0.90 (8.27 ± 1.56)
East Asia	1.46 ± 0.11 (2.46 ± 0.38)	-4.21 ± 1.54 (-10.24 ± 5.18)	1.39 ± 2.29 (7.56 ± 4.34)	0.95 (0.79)	2.28 ± 1.87 (9.22 ± 5.19)

Note. The units of intercept, MB, and RMSE are ppbv. the boldface means the best agreements with in situ observations. The ranges are standard deviation.

Table 6

Daytime Mean Surface NO₂ Concentrations (8–20LT) and Diurnal Difference of NO₂ Between Morning (10LT) and Early Afternoon (14LT) at Selected Large Cities Derived From In Situ Observations, and Relative Biases Against the Observations in the Model Simulation and Data Assimilation During June 29 to July 21, 2008

City	Daytime mean concentration (8–20LT)			Ratio of 10–14LT		
	Obs. (ppbv)	CTL bias (%)	ASSIM bias (%)	Obs.	CTL bias	ASSIM bias
Europe						
Athens	2.80	95.9	35.3	1.19	−0.46	−0.45
Brussels	4.15	46.7	−23.1	1.17	−0.02	−0.11
Berlin	2.52	99.9	14.9	1.28	−0.37	−0.23
Lisbon	4.72	−15.3	−36.9	1.53	−0.37	−0.57
London	5.38	45.6	−21.5	0.94	0.04	0.09
Madrid	2.55	20.4	−18.1	1.11	0.10	0.13
Paris	4.12	56.5	−7.2	0.90	0.60	−0.04
Rome	1.35	160.8	139.4	3.49	−2.73	−2.72
Vienna	2.79	85.8	8.3	1.43	−0.21	−0.39
The United States						
Chicago	8.82	140.7	−42.4	0.76	0.74	0.20
Dallas	2.54	286.9	−17.5	1.09	0.18	−0.06
Detroit	3.11	449.8	8.7	0.91	−0.03	−0.15
Los Angeles	12.79	34.4	−9.0	1.44	0.39	0.07
Miami	2.37	39.5	−20.3	0.62	0.02	0.27
New York	8.58	232.7	86.0	1.08	−0.003	−0.008
Philadelphia	5.29	77.0	3.2	1.11	0.59	0.54
Phoenix	4.46	63.2	−29.8	1.29	0.63	0.19
East Asia						
Hong Kong	16.39	73.1	19.0	1.00	−0.09	−0.15
Tokyo	12.62	102.2	−2.2	1.17	0.07	0.14

Note. The boldface means the best agreements with in situ observations.

explained by corrections made to ozone and CO concentrations in a sensitivity assimilation calculation without OMI, GOME-2, and SCIAMACHY NO₂.

4.2.2. Validation Using Ozonesonde Observations

Vertical ozone profiles were validated using ozonesonde observations (Figure 4). Positive model bias of ozone was commonly found through the extratropical troposphere during the boreal summer, which can be associated with various factors including vertical mixing and inflow from the stratosphere, precursor concentrations and chemistry, and dry deposition. Large positive model biases (by up to a factor of 2) in the upper troposphere can partly be attributed to the model overestimation in the vertical transport; residual vertical velocity at 15 km altitude was larger by 38% compared to ERA-Interim over the extratropics in the southern hemisphere. According to the results of a free-running model calculation (i.e., without the meteorological nudging) using the CHASER model, about half of the model overestimation in residual vertical velocity was attributed to the meteorological nudging process. Another possible error source is the catalytic ozone loss due to halogen species. We confirmed positive model bias reductions of 9%–53% by incorporating appropriate upper boundary of chloride and bromine species obtained from the CCM1 REFC1 run of CCSR/NIES CCM (Akiyoshi et al., 2009, 2016; Morgenstern et al., 2016) and detailed treatments in tropospheric bromine chemistry in a sensitivity model calculation.

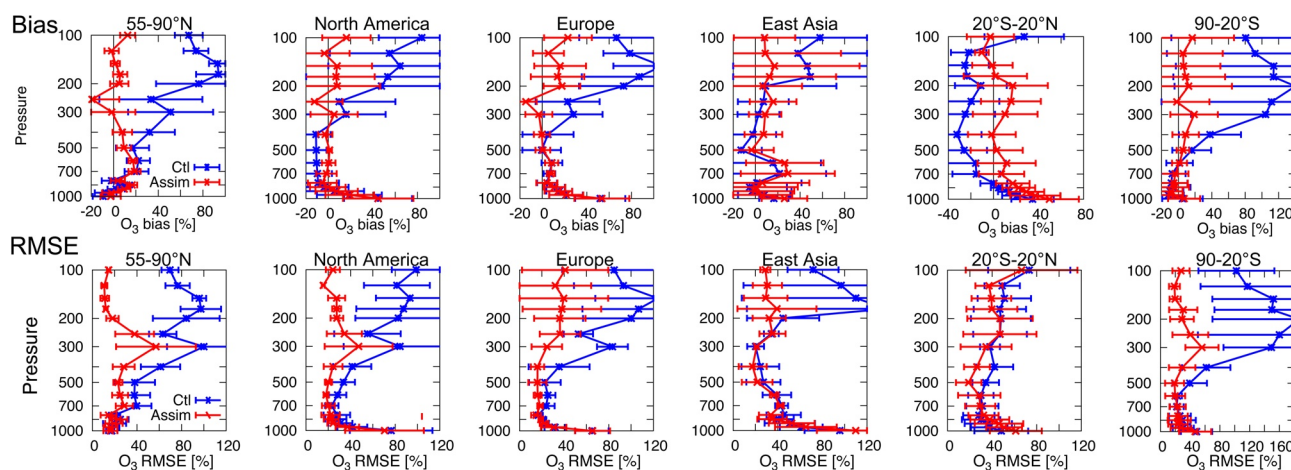


Figure 4. Vertical profiles of ozone mean bias (top), and RMSE for individual profiles (bottom) derived from ozonesonde observations, model simulation, and data assimilation at ozonesonde locations over the northern high latitude (55°N–90°N; the first column), North America (20°N–55°N; the second column), Europe (20°N–55°N; the third column), East Asia (20°N–55°N; the fourth column), the tropics (20°S–20°N; the fifth column), and the southern mid-high latitudes (90°S–20°S; the sixth column) during June 29 to July 21, 2008. The unit is %. The error bars are standard deviation of O₃ time series.

These model biases were greatly reduced by data assimilation. In the upper troposphere, the positive model bias was reduced by 25%–93% at 200 hPa in the extratropics, with statistical significance at the 95% level for many cases. In the middle troposphere, the positive model bias was reduced by 45% and 65% at 500 hPa over the northern high latitudes (55°N–90°N) and the southern mid-high latitudes (20°S–90°S), respectively, whereas these differences were not statistically significant. The negative model biases over North America, East Asia, and the tropics were reduced by more than 70%, with statistical significance at the 95% level over North America and the tropics. The RMSEs in the upper and middle troposphere were also greatly reduced over most regions. In the lower troposphere below 850 hPa, in contrast, large RMSEs remained over the northern midlatitudes and the tropics. The remaining errors suggest a requirement of further observational constraints (e.g., VOC emission optimization from the assimilation of formaldehyde retrievals) and model process improvements. The multiconstituent data assimilation, including the precursors' emission optimization, was important to improve the entire tropospheric profile of ozone as demonstrated by our previous studies (Miyazaki et al., 2015; Miyazaki, Sekiya, et al., 2019).

4.2.3. Validation Using ARCTAS-B Aircraft-Campaign Observations

Figure 5 compares the vertical profiles of ozone, NO₂, HNO₃, PAN, OH, and HO₂ with the ARCTAS-B aircraft observations from June 29 to July 13, 2008 after the spin-up period. Fresh Canadian fire plumes were filtered out based on the results presented by Simpson et al. (2011) to evaluate data assimilation performance under regional background conditions. The model simulation and data assimilation did not capture the fresh Canadian fire plumes (figure not shown), because monthly mean-based biomass burning emissions were used as a priori and satellite retrievals were not available over most of the plumes. Nevertheless, the model resolution of 0.56° would help resolve large-scale (>50 km) fire plumes. The model simulation considerably overestimated the observed ozone concentrations in the upper troposphere, as commonly found in the validation against the ozonesonde measurements (cf., Section 4.2.2). The model simulation overestimated NO₂ near the surface and underestimated it in the free troposphere, while underestimating HNO₃ and PAN in the free troposphere. These model biases could be attributed to the uncertainties in surface and lightning NO_x sources and the chemical conversion of NO₂ to nitrogen reservoirs (e.g., HNO₃ and PAN) in the model simulation. The large negative OH model bias can be related to the conversion reaction of HO₂ + NO to OH + NO₂, because the model simulation considerably underestimated OH/HO₂ ratio compared with the aircraft observations.

The positive ozone model biases were reduced above 500 hPa by data assimilation with statistical significance at the 98% confidence level, but increased slightly below 600 hPa. The negative NO₂ model bias above 600 hPa was reduced by 50%–73%, while the positive model bias near the surface was reduced by 83%, which were statistically significant at the 98% level. The remaining positive bias in near-surface NO₂ could

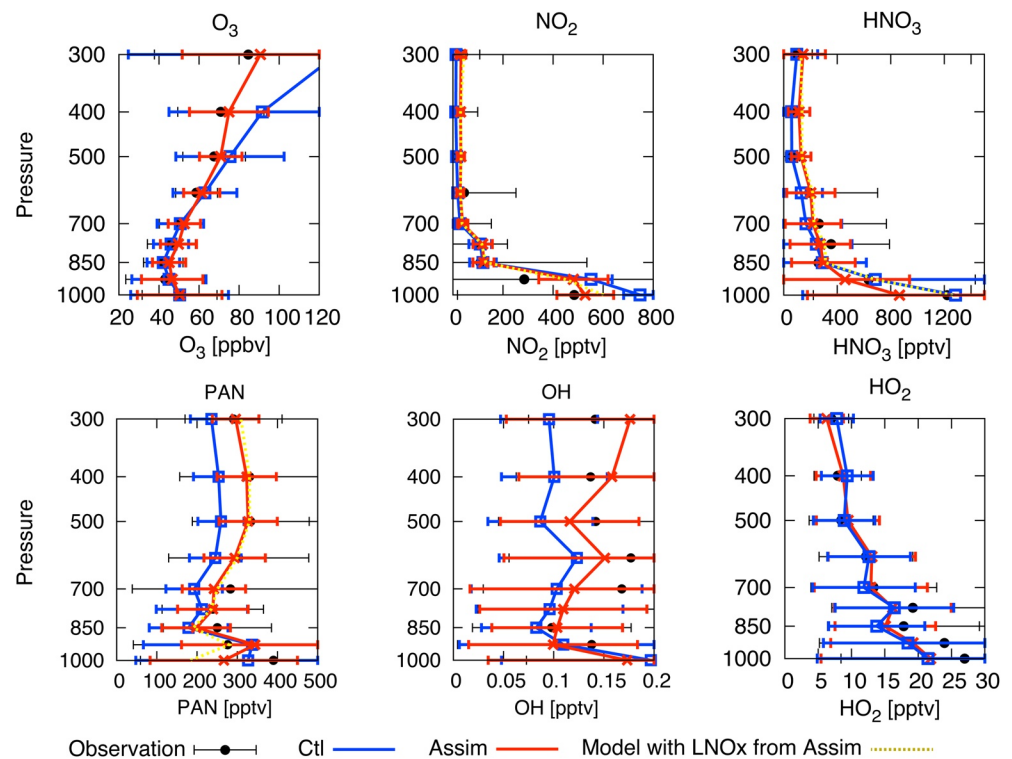


Figure 5. Vertical profiles of ozone (upper left), NO_2 (upper middle), HNO_3 (upper right), PAN (lower left), OH (lower middle), and HO_2 (lower right) concentrations derived from the ARCTAS-B aircraft-campaign observations, model simulation, and data assimilation during June 29 to July 13, 2008. The units of ozone and other species are ppbv and pptv, respectively. The red, blue, and yellow lines are results from the data assimilation, the control model simulation, and the model simulation with lightning NO_x sources estimated by the data assimilation. The error bars are standard deviation of individual samples.

explain the positive ozone bias in the lower troposphere. The negative model biases in HNO_3 were reduced by 30%–85% between 600 and 800 hPa, whereas these differences were statistically insignificant. Below 850 hPa, HNO_3 concentrations became too low. For PAN, the negative model biases were mostly removed above 850 hPa with statistical significance at the 98% confidence level. These bias reductions in the free tropospheric NO_2 , HNO_3 , and PAN were mainly due to increased lightning NO_x . By applying the optimized lightning NO_x fields from data assimilation in a model simulation, we confirmed that the negative model biases of NO_2 , HNO_3 , and PAN can be reduced by more than 73%, 50%, and 75%, respectively, above 700 hPa. The negative OH model biases were reduced by 11%–81% between 400 and 900 hPa, with statistical significance at the 98% level above 600 hPa, associated with increased HO_x production and HO_2 to OH conversions through data assimilation adjustments to ozone and NO_2 concentrations. The negative and positive HO_2 model biases were slightly reduced below and above 400 hPa, respectively, whereas these differences were not statistically significant.

4.3. Impacts of Increasing Horizontal Resolution

4.3.1. Tropospheric NO_2 Column

As summarized in Table 7, increasing the horizontal resolution from 2.8° to 0.56° improved the model performance over polluted regions, with the RMSE reduction against OMI NO_2 by 5%, 8%, and 12%, over Europe, the United States, and China, respectively, while the reductions were statistically insignificant. Over India, the improvements in regional-mean RMSE were not evident, because of increased positive biases over Delhi and power plants. Over these polluted regions, the RMSE reductions owing to data assimilation at 0.56° resolution were larger than those at 1.1° and 2.8° resolutions by factors of 1.2–3 and 1.5–3, respectively. The RMSEs after data assimilation at 0.56° resolution were smaller by 5%–24% and 0%–34%

Table 7

Mean Bias (MB), Spatial Correlation Coefficient (S-Corr.), and Root Mean Square Error (RMSE) for Mean Concentration Fields of Tropospheric NO₂ Column Compared With OMI in the Data Assimilation and Model Simulation (in Brackets) at 0.56°, 1.1°, and 2.8° Resolutions During June 29 to July 21, 2008

Resolution	0.56°	1.1°	2.8°
MB			
Global	−0.06 ± 0.01 (−0.21 ± 0.01)	−0.04 ± 0.01 (−0.20 ± 0.05)	−0.04 ± 0.01 (−0.21 ± 0.02)
Europe	0.07 ± 0.07 (−0.20 ± 0.11)	0.14 ± 0.09 (−0.07 ± 0.07)	0.14 ± 0.08 (−0.12 ± 0.05)
The United States	0.03 ± 0.05 (−0.13 ± 0.12)	0.12 ± 0.10 (−0.03 ± 0.07)	0.07 ± 0.08 (−0.11 ± 0.04)
China	0.05 ± 0.20 (−0.14 ± 0.11)	0.14 ± 0.11 (−0.12 ± 0.07)	0.11 ± 0.09 (−0.21 ± 0.04)
India	0.01 ± 0.09 (−0.14 ± 0.12)	0.08 ± 0.10 (−0.15 ± 0.09)	0.06 ± 0.11 (−0.15 ± 0.05)
S-Corr.			
Global	0.91 (0.85)	0.90 (0.85)	0.88 (0.82)
Europe	0.87 (0.84)	0.86 (0.82)	0.81 (0.75)
The United States	0.89 (0.87)	0.87 (0.84)	0.84 (0.77)
China	0.94 (0.91)	0.91 (0.87)	0.87 (0.82)
India	0.89 (0.78)	0.84 (0.81)	0.90 (0.85)
RMSE			
Global	0.24 ± 0.06 (0.39 ± 0.04)	0.25 ± 0.03 (0.38 ± 0.02)	0.28 ± 0.05 (0.39 ± 0.02)
Europe	0.39 ± 0.09 (0.46 ± 0.09)	0.41 ± 0.09 (0.45 ± 0.04)	0.46 ± 0.10 (0.52 ± 0.04)
The U.S.	0.30 ± 0.09 (0.42 ± 0.08)	0.36 ± 0.09 (0.43 ± 0.04)	0.37 ± 0.10 (0.44 ± 0.04)
China	0.55 ± 0.68 (0.89 ± 0.25)	0.69 ± 0.22 (0.92 ± 0.03)	0.83 ± 0.26 (0.97 ± 0.03)
India	0.29 ± 0.06 (0.50 ± 0.10)	0.38 ± 0.09 (0.45 ± 0.04)	0.29 ± 0.07 (0.36 ± 0.04)

Note. All statistics were calculated at 0.56°-bin Grid. The unit of MB and RMSE is $\times 10^{15}$ molecules cm^{-2} . The boldface means the best agreements with in-situ observations. The ranges of MB and RMSE are standard deviation of time series.

than at 1.1° and 2.8° resolutions, respectively, with statistical significance at the 90% level using the *U*-test, except for India. Similar resolution sensitivity in data assimilation improvements at both megacity and global scales were found in comparisons against the GOME-2 and SCIAMACHY retrievals (not shown).

Figure 6 compares the tropospheric NO₂ column in megacities worldwide. For the comparison, the tropospheric NO₂ column was averaged within 50 km from selected points (i.e., megacities) while applying a distance-based weight function (i.e., the inverse of the distance was applied to each retrieval). By increasing the horizontal resolution from 2.8° to 0.56°, the RMSE for the simulated NO₂ concentrations was reduced by 31% and the slope was increased from 0.51 to 1.44, while these differences were statistically significant. The data assimilation at 0.56° resolution reduced the RMSE by 16%, which was larger than the RMSE reductions at the coarser resolutions by up to a factor of two. The data assimilation at 0.56° resolution became the slope closer to 1 (from 1.44 to 0.81) with statistical significance at the 98% level, whereas the slopes at 1.1° and 2.8° resolution were degraded and insignificantly changed, respectively, by the data assimilation. The RMSE after data assimilation at 0.56° resolution was 7%–35% smaller than at the coarser resolutions, owing to the large negative bias reductions over megacities in China (more than 35%), such as Beijing, Shanghai, and Guangzhou. These differences in RMSEs obtained from the model simulation and data assimilation at different resolutions were statistically significant at the 95% confidence level using the *t*-test and *U*-test.

4.3.2. Tropospheric Ozone

In the model simulation, surface ozone concentrations were generally increased by 14%–40% over the southern mid-high latitudes, northern high latitudes, the Pacific, and the Atlantic owing to the increase in resolution from 2.8° to 0.56° (Figure 7). Over Europe, the United States, and East Asia, surface ozone concentrations were reduced by 7%–12% from 2.8° to 1.1° resolution, whereas it was slightly increased from 1.1° to 0.56° resolution. Over remote regions, the increase in surface ozone concentrations with resolution was

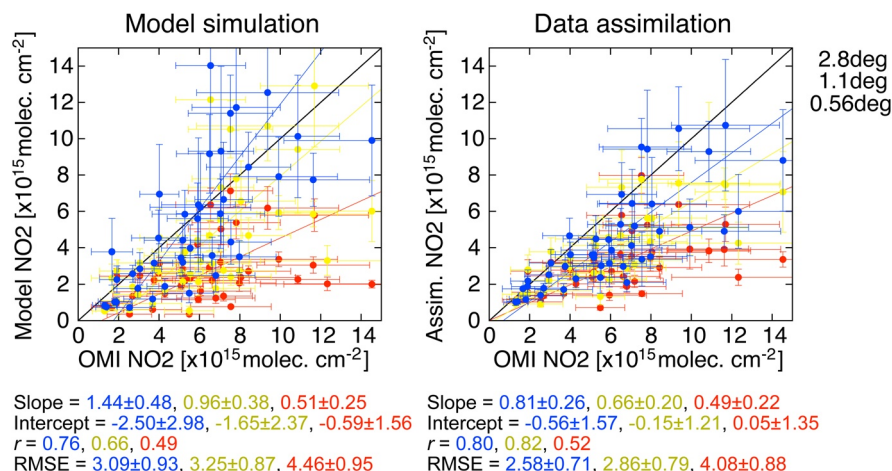


Figure 6. Scatter plots of tropospheric NO_2 column ($\times 10^{15}$ molecules cm^{-2}) at megacities (>10 million of population) over the globe from OMI, the model simulation (left), and data assimilation with 32 ensembles (right) at 0.56, 1.1, and 2.8° resolutions during June 29 to July 21, 2008. The blue, yellow, and red circles are data assimilation at 0.56°, 1.1°, and 2.8° resolutions, respectively. The values and mean retrieval errors are averages within a 50 km distance from each city, with a weighting function application based on the inverse of the distance from each city. The mean retrieval errors are calculated using Equation 9, but the inverse of the distance from each city was used as the weighting function. The error bars are standard deviation of NO_2 time series.

mostly explained by the increase in ozone tracer concentrations of stratospheric origin (Sekiya et al., 2018). Over major polluted regions, weaker chemical ozone production at 0.56° resolution (by 18%–25%) than 2.8° resolution led to the decrease in surface ozone, which could be attributed to suppressed instantaneous mixing of ozone precursors in grid cells and resolving different ozone chemical regimes (i.e., NO_x - or VOC-limited). These differences over most regions were statistically significant at the 95% confidence level determined by two-sample *t*-test using temporal variances. Compared with the surface measurements, the RMSEs for ozone were reduced by 8%–24% by increasing the horizontal resolution from 2.8° to 1.1° over most regions except over the tropics (Table 8). Additional RMSE reductions were obtained by increasing the resolution to 0.56° for many regions except over Europe and East Asia. These RMSE reductions by increasing resolutions were statistically significant at the 95% level. Over the northern high latitudes and the southern mid-high latitudes, the increase in ozone tracer concentrations of stratospheric origin largely contributed to the total improvements against the in situ observations (by more than 85%).

The data assimilation at all resolutions increased surface ozone concentrations over most remote and rural regions (by 3%–5% on average), and decreased over polluted regions and Central Africa, with statistical significance at the 95% confidence level determined by two-sample *t*-test using temporal variances. The changes owing to the data assimilation were smaller at 0.56° and 1.1° resolutions than at 2.8° resolution over most regions. Improvements in the agreements against the in situ observations by data assimilation were greater at 0.56° resolution than at 1.1° and 2.8° resolutions over the United States. The model resolution dependence of data assimilation improvement was smaller over East Asia and the remote regions over the extratropics. The RMSEs after data assimilation became significantly smaller with increasing model resolution over most regions. The surface ozone changes after data assimilation over most regions with the changes larger than 2 ppbv were statistically significant at the 95% confidence level determined by two-sample *t*-test using temporal variances.

Data assimilation at 0.56° resolution resolves urban-rural contrasts of surface ozone and captures the observed concentrations in the city center of Los Angeles (5% positive bias) obtained from the AQS database (Figure 8), which would benefit health impact assessments. We evaluated data assimilation products for ozone exposure on a large scale (i.e., 2.8°) using the population-weighted concentration, which is a commonly used metric of health impacts (e.g., WHO, 2016). The weighting function applied in this study was based on population density (CIESIN, 2018, obtained through <http://sedac.ciesin.columbia.edu>). Over Los Angeles, the population-weighted ozone concentration after data assimilation was 33% smaller at 1.1°

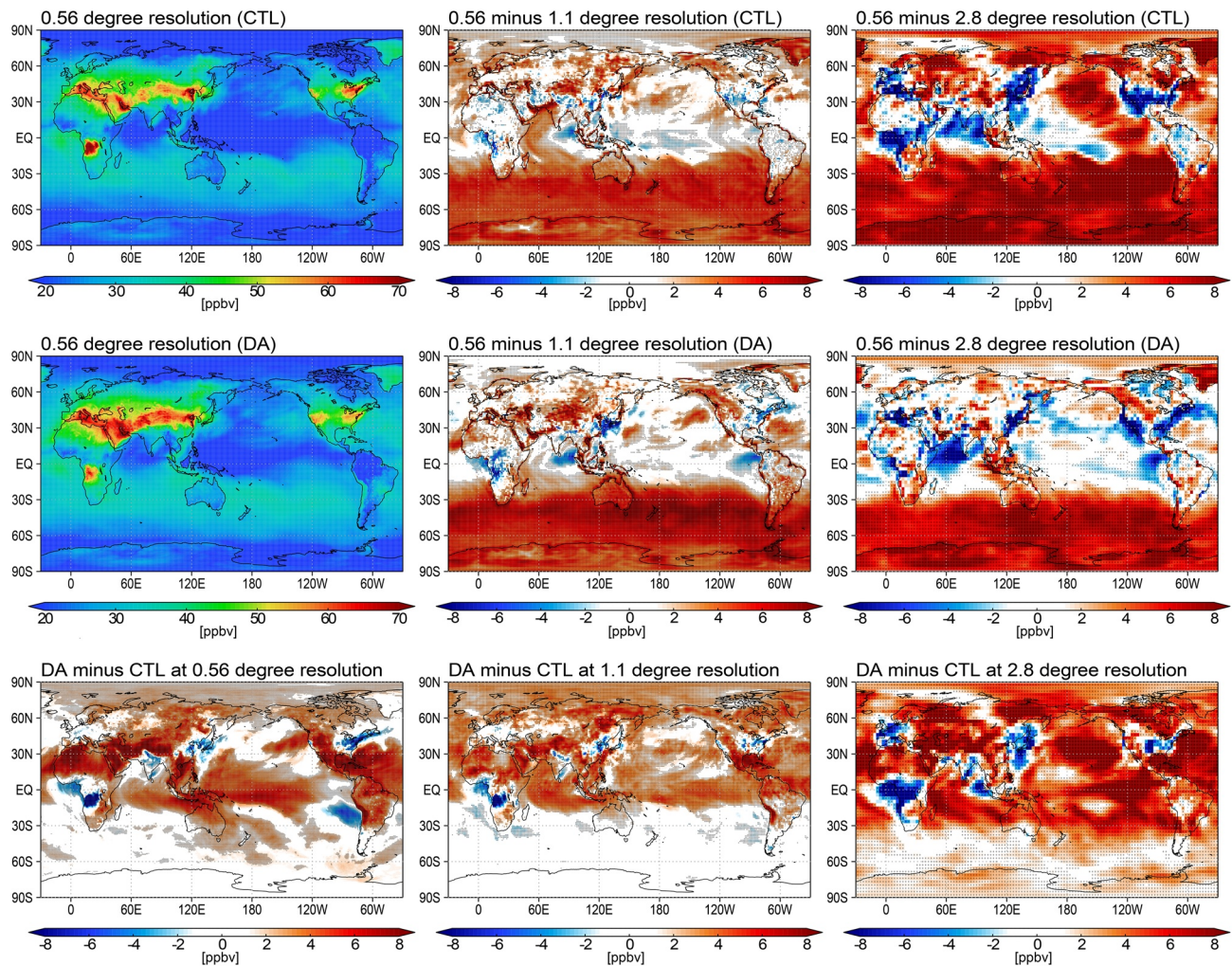


Figure 7. Global distribution of surface ozone concentrations (ppbv) derived from the model simulation at 0.56° resolution (upper left) and the differences between 0.56° and 1.1° resolutions (upper middle) and between 0.56° and 2.8° resolutions (upper right) during June 29 to July 21, 2008. Lower panels show differences in surface ozone concentrations (ppbv) between the data assimilation and the model simulation at 0.56° resolution (lower left), 1.1° resolution (lower middle), and 2.8° resolution (lower right). The grids with open circle indicate that the mean differences of ozone concentrations (upper column) and the changes made by data assimilation (lower column) from those at 0.56° resolution are statistically significant at the 95% confidence level using the two-sample *t*-test.

resolution than at 2.8° resolution with statistical significance at the 95% confidence level, whereas the differences between 0.56 and 1.1° resolution were insignificant (−9%). Over Shanghai, the differences in population-weighted ozone concentrations between all three resolutions were negligible.

In the free troposphere (figure not shown), by increasing the horizontal resolution from 2.8° to 0.56°, the RMSEs against the ozonesonde measurements over North America were decreased by 19% at 800 hPa and were increased by 46% at 200 hPa. The effects of model resolution on the model performance of free tropospheric ozone were greatly reduced by data assimilation in the multi-constituent data assimilation framework, as consistently revealed by Miyazaki, Bowman, Yumimoto, et al. (2020). Nevertheless, the ozone analysis after data assimilation was smallest at 0.56° resolution, with the RMSEs being smaller by 2%–23% than at 2.8° resolution for the entire troposphere.

Table 8

Mean Bias (MB) and Root Mean Square Error (RMSE) for Mean Surface Concentrations of Ozone Obtained From the Data Assimilation and the Model Simulation (in Brackets) at 0.56°, 1.1°, and 2.8° Resolutions Compared to the Rural In Situ Measurements Over the Globe

Resolution	0.56°	1.1°	2.8°
MB			
Europe	8.27 ± 2.49 (7.64 ± 3.08)	7.92 ± 2.58 (5.63 ± 2.61)	8.87 ± 2.90 (9.51 ± 4.50)
The United States	11.04 ± 2.38 (12.53 ± 2.37)	13.22 ± 2.61 (13.32 ± 2.04)	14.68 ± 2.80 (13.83 ± 3.04)
East Asia	11.44 ± 2.17 (13.42 ± 2.29)	11.08 ± 3.17 (10.07 ± 2.51)	10.91 ± 3.56 (15.41 ± 5.49)
NH other	0.48 ± 2.41 (−2.41 ± 3.14)	−2.07 ± 2.23 (−5.25 ± 2.91)	−2.89 ± 2.53 (−7.04 ± 2.03)
Tropics	9.91 ± 1.82 (5.53 ± 2.37)	8.97 ± 1.89 (6.02 ± 2.01)	9.76 ± 1.29 (4.53 ± 1.72)
SH	−3.34 ± 2.26 (−4.18 ± 2.99)	−10.51 ± 1.73 (−10.43 ± 1.79)	−10.43 ± 2.01 (−11.56 ± 0.64)
RMSE			
Europe	12.68 ± 2.31 (12.20 ± 2.02)	12.68 ± 2.49 (11.32 ± 2.36)	13.77 ± 3.42 (15.04 ± 3.16)
The United States	12.86 ± 1.75 (15.72 ± 1.98)	15.99 ± 2.59 (17.05 ± 2.05)	18.42 ± 2.50 (18.57 ± 3.10)
East Asia	14.39 ± 1.83 (17.09 ± 2.55)	16.78 ± 2.73 (15.90 ± 2.73)	14.81 ± 2.36 (18.45 ± 3.52)
NH other	4.01 ± 1.51 (4.25 ± 1.97)	4.34 ± 1.91 (6.61 ± 2.23)	4.59 ± 2.05 (7.61 ± 2.04)
Tropics	11.81 ± 1.58 (9.88 ± 1.83)	11.57 ± 1.75 (10.23 ± 1.65)	11.53 ± 1.62 (8.85 ± 2.06)
SH	9.40 ± 1.23 (9.44 ± 1.14)	12.94 ± 1.10 (13.05 ± 1.96)	14.20 ± 1.06 (15.20 ± 1.31)

The unit is ppbv. The bold face means the best agreements with in situ observations. The ranges are standard deviation of time series.

5. Emission Estimates

5.1. Global and Regional Emissions

The developed system provides globally consistent information on NO_x and CO emissions on a megacity scale. As summarized in Figure 9 and Table 9, the regional a posteriori NO_x emissions differed considerably from the a priori emissions over polluted and biomass burning regions, with statistical significance at the 95% confidence level over most of regions. Strong positive increments (by 58% on average) were found over regions where soil emissions are dominant (>50%), such as over Spain, Turkey, the Midwest United States, Kazakhstan, and the Sahel region. By assuming that a ratio of the soil emissions to total emissions in the a priori emissions maintains in the a posteriori emissions at each grid cell, the global amount of the a posteriori soil emissions increased by 17% (to 10.2 Tg N yr^{−1}), which was slightly smaller than the estimates of annual total soil emissions reported by Hudman et al. (2012) (10.7 Tg N yr^{−1}) and Vinken et al. (2014) (12.6 Tg N yr^{−1}).

The analysis increments of NO_x emissions were mostly negative over northern Europe (by 15% for 46°N–60°N) and positive over Southern Europe (by 20% for 35°N–46°N) on regional scales (Figure 10). Over large urban areas in Europe, the negative increments were larger than 30% (Table 10), in contrast to the positive increments over remote areas of Southern Europe, which suggest underestimated soil emissions, as similarly suggested by Vinken et al. (2014) and Zyrichidou et al. (2015). The a posteriori ship emissions increased to 0.77 Tg N yr^{−1} by 33% over Europe, which is 26% smaller than the 1.04 Tg N yr^{−1} of annual mean emissions in 2008 estimated by Boersma et al. (2015).

Over the eastern United States, the analysis increments of NO_x emissions are mostly negative (by 28% for 71°W–95°W in average). Positive increments were found over rural areas of the western United States, associated with the underestimated soil emissions (Oikawa et al., 2015; Weber et al., 2015), in contrast to strong negative increments in large urban areas.

Over East Asia, the country's total NO_x emissions were decreased by 22%, 20%, and 24% in China, Korea, and Japan, respectively. The emissions also increased over rural areas in the northern part of Inner Mongolia (by 19%) and Heilongjiang province (by 12%), whereas the emissions decreased over most of the large

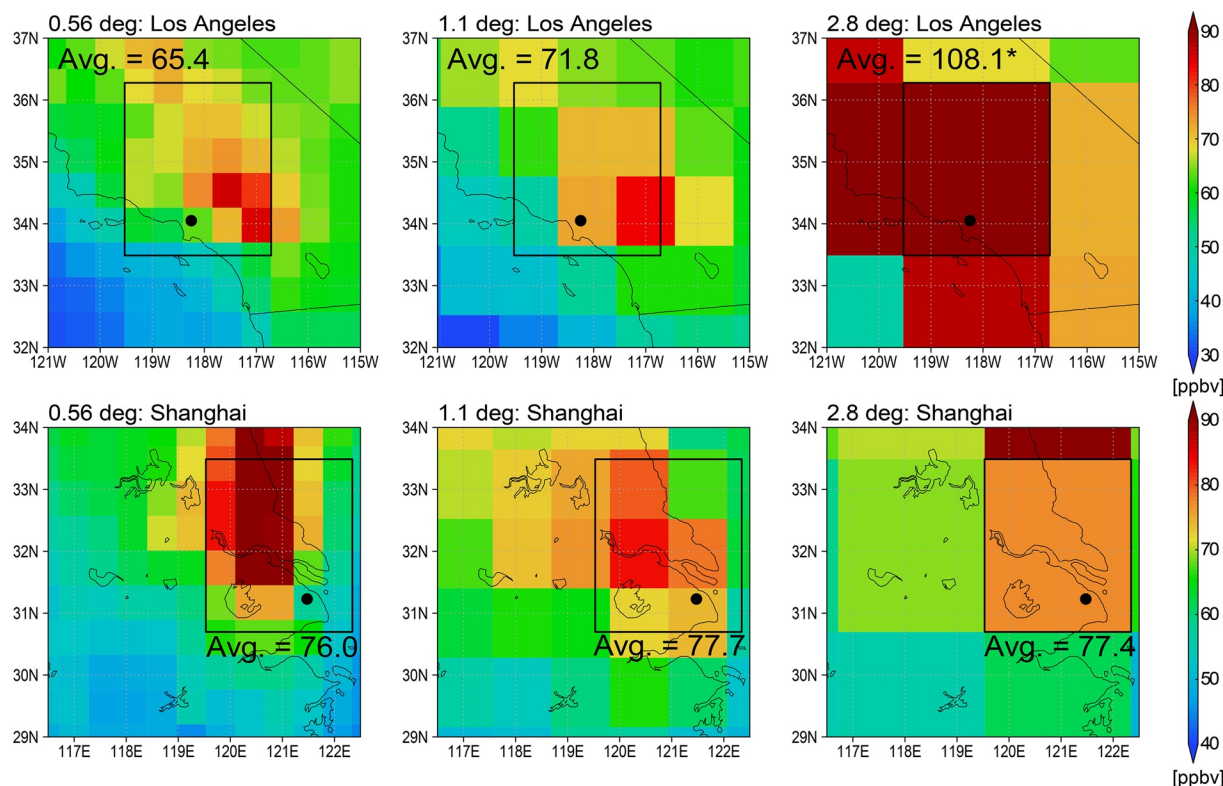


Figure 8. Spatial distribution of daytime-mean (8–20 LT) surface ozone concentrations (ppbv) around Los Angeles (upper row) and Shanghai (lower row) derived from data assimilation with 32 ensembles at 0.56° (left column), 1.1° (middle column), and 2.8° (right column) resolutions during June 29 to July 21, 2008. “Avg.” means the population-weighted average ozone with analysis spread in the solid square. The asterisk indicates that difference of “Avg” from that at 0.56° resolution is statistically significant at the 95% confidence level using the two-sample *t*-test.

urban areas, except for large increases over Shenzhen, Busan, and Osaka. Our estimate of 7.5 Tg N yr^{-1} over China (102°E – 132°E , 18°N – 50°N) is comparable to the top-down estimate of 7.8 Tg N yr^{-1} for July 2008 using the DECSO system and the OMI QA4ECV retrievals (Ding et al., 2018, obtained from <http://www.globemission.eu/index.php>).

Over India, the spatial distribution of NO_x emissions was considerably modified, with larger decreases over southern India (by 31% for 8°N – 18°N) than over northern India (by 15% for 18°N – 35°N). Substantial emission reductions were found in large urban areas in India, as well as over large-scale coal-fired power plants (by 24%–65%) in the state of Chhattisgarh, Jharkhand, and the West Bengal (the locations were taken from Lu and Streets (2012)). The overestimations of the bottom-up emissions for the urban areas in India were commonly suggested by the regional modeling study (Karambelas et al., 2018). Ship emissions over the eastern Indian Ocean were increased by 40%. Urban area emissions in Southeast Asia increased largely except over Kuala Lumpur.

MODIS measured biomass burnings during April over the Mainland of Southeast Asia. Bottom-up biomass burning emissions are commonly constructed from burned area fractions (BAFs) obtained from satellite observations and emission factors measured in laboratories. Meanwhile, previous studies using top-down emission estimates inferred from OMI reported close relationship between NO_x emissions and fire radiative power (FRP) (e.g., Mebust & Cohen, 2014), owing to the more efficient oxidation of fuel-content nitrogen at high combustion temperature. Thus, we evaluated the estimated CO and NO_x emissions during the events using the MODIS BAF obtained from the GFED4 data set (Giglio et al., 2013) and FRP obtained from the Collection 6 MODIS active fire products (Giglio, 2015) (Figure 11). Data assimilation increased the CO and NO_x emissions by a factor of 2 and 1.5, respectively, over the major burning region (the rectangle in Figure 11). The a priori NO_x emissions were spatially correlated better with BAF ($r = 0.30$) than FRP

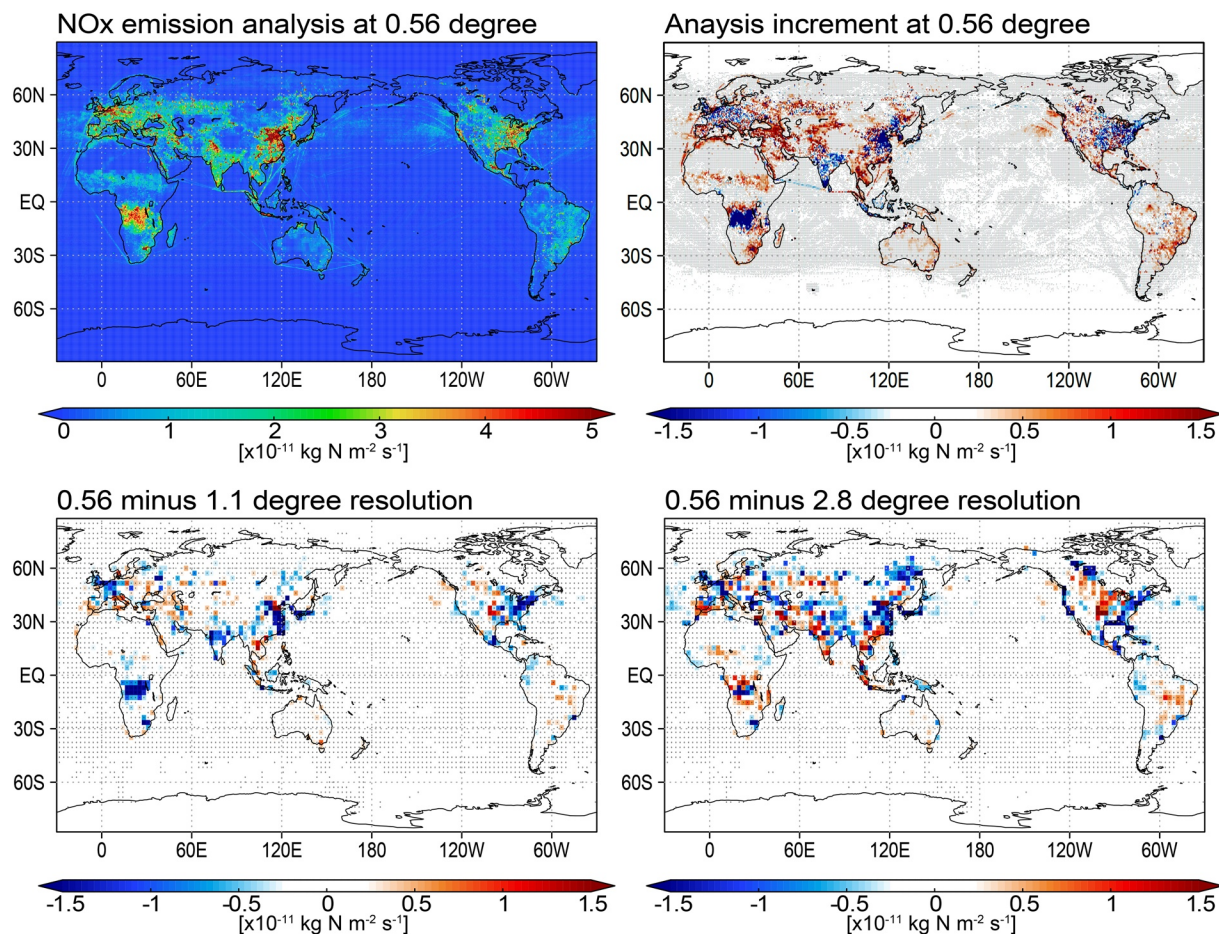


Figure 9. Global distribution of a posteriori surface NO_x emission from 0.56°-resolution data assimilation with 64 ensembles (upper left) and the difference between the a posteriori and a priori emissions (upper right) during June 29 to July 21, 2008. The differences in the a posteriori emissions from the data assimilation with 32 ensembles between 0.56° and 1.1° resolutions (lower left) and between 0.56° and 2.8° resolutions (lower right) are also shown. The unit is $\times 10^{-11}$ kg N m⁻² s⁻¹. The emissions are mapped onto a 2.8°-bin grid. The grids with open circle indicate that mean differences of a posteriori emissions from those at 0.56° resolution are statistically significant at the 95% confidence level using the two-sample *t*-test.

Table 9

Regional Amounts of the a Priori and a Posteriori Surface NO_x Emissions (Tg N yr⁻¹) During June 29 to July 21, 2008. *N* Denotes Ensemble Size

	A priori	0.56° resolution		1.1° resolution	2.8° resolution
		<i>N</i> = 64	<i>N</i> = 32	<i>N</i> = 32	<i>N</i> = 32
Global	49.9	51.0	51.5	56.1	56.8
Europe	4.6	4.6	4.7	4.8	4.9
The United States	6.4	5.1	5.3	6.2	5.9
China	9.6	7.5	7.7	8.9	8.8
India	3.3	2.6	2.6	3.2	2.7
Southeast Asia	0.7	1.3	1.3	1.1	1.2
West Asia	2.4	3.5	3.5	3.5	3.3
Central Africa	6.3	4.0	4.0	5.4	3.7
South Africa	0.4	0.3	0.3	0.5	0.4

($r = 0.23$), whereas the a posteriori emissions were correlated better with FRP ($r = 0.42$) than BAF ($r = 0.36$). These results confirm that FRP is a better indicator of NO_x emissions from biomass burning than BAF.

5.2. Impacts of Increasing Horizontal Resolution

As shown in Figure 9 and summarized in Table 9, the a posteriori global total NO_x emission was 51.5 Tg N yr⁻¹ at 0.56° resolution, which was 8%–9% smaller than at 1.1° and 2.8° resolutions. The regional total emissions at 0.56° resolution were 2%–26% smaller than those at 2.8 and 1.1° resolutions over polluted regions, such as Europe, the United States, China, India, and South Africa. The changes in the a posteriori emissions with model resolution over most regions were statistically significant at the 95% confidence level determined by two-sample *t*-test using temporal variances. The model resolution effects on the emission analysis increments varied with emission strength. Over medium and strong sources ($> 3 \times 10^{-11}$ kg N m⁻² s⁻¹), the estimated global total emissions at 0.56° resolution were smaller than those at 1.1° and 2.8° resolutions by 15%, while mean differences were statistically insignificant over weak sources

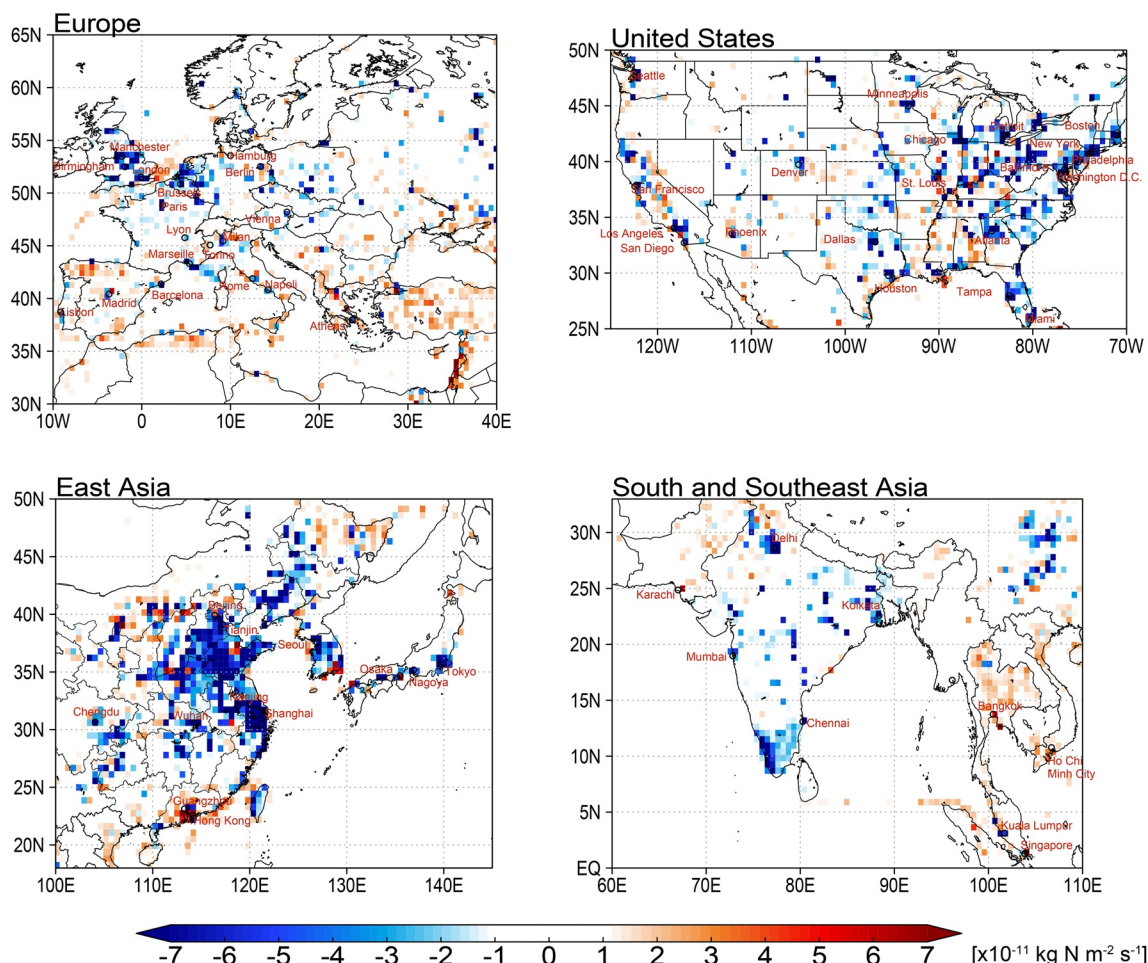


Figure 10. Regional distributions of the difference between the a posteriori and a priori surface NO_x emissions derived from 0.56° -resolution data assimilation with 64 ensembles over Europe (upper left), the United States (upper right), East Asia (lower left), and South and Southeast Asia (lower right) during June 29 to July 21, 2008. The unit is $\times 10^{-11} \text{ kg N m}^{-2} \text{ s}^{-1}$. The emissions are mapped onto a 0.56° -bin grid.

($< 3 \times 10^{-11} \text{ kg N m}^{-2} \text{ s}^{-1}$) except over ship lanes in the northern Pacific and Atlantic, where the estimated emissions at 0.56° resolution were 5%–7% smaller than those at 1.1° and 2.8° resolutions.

Figure 12 compares NO_x emissions over Los Angeles and Shanghai obtained from the data assimilation at 0.56° , 1.1° , and 2.8° resolutions. Over the 2.8° -bin grid domain (the rectangle of Figure 12), the emission estimate in Los Angeles was reduced by 32% from 2.8° to 1.1° resolution and by 12% from 1.1° to 0.56° resolution. In Shanghai, the emission estimate was reduced by 17% from 1.1° to 0.56° resolution. The reduction with increasing model resolution from 2.8° to 0.56° over Los Angeles was statistically significant at the 95% confidence level, while the reductions over Shanghai were statistically insignificant. NO_x emissions were statistically significantly decreased with increasing resolution over 25 of selected 42 megacities like those over Los Angeles, while insignificant changes like those over Shanghai were found over the other 17 megacities.

6. Discussion

6.1. Importance of Horizontal Resolution on Concentration Analysis

The model simulations at 0.56° resolution, that did not use data assimilation, improved the agreement with OMI for tropospheric NO_2 and with ozonesonde observations for tropospheric ozone, compared to the model simulations at 2.8° resolution for many cases. As discussed in Sekiya et al. (2018), these improvements

Table 10
NO_x Emission Analysis Increments (%) in Large Cities Over Europe, the United States, and Asia

Region	City	Increment
Europe	London	−50
	Brussels	−59
	Paris	−46
	Barcelona	−68
	Milan	−49
	Rome	−30
	Athens	−42
The United States	New York	−45
	Los Angeles	−29
	Philadelphia	−46
	Chicago	−79
	Detroit	−85
	Dallas	−77
	Atlanta	−54
East Asia	Beijing	−4
	Shanghai	−47
	Hong Kong	−29
	Chengdu	−64
	Shenzhen	19
	Seoul	−31
	Busan	47
	Tokyo	−50
	Osaka	48
South Asia	Delhi	−68
	Kolkata	−77
	Mumbai	−40
	Chennai	−59
Southeast Asia	Ho Chi Minh City	88
	Singapore	47
	Bangkok	48
	Kuala Lumpur	−55

were caused by closer spatial representativeness between observations and model simulation and better representation of large-scale processes through the consideration of the small-scale processes (e.g., nonlinear chemistry, stratosphere-troposphere exchange). The improvements in a priori information can partly contribute to improvements in agreements of data assimilation analysis with assimilated and independent observations.

The data assimilation at 0.56° resolution reduced RMSEs for tropospheric NO₂ column against the satellite observations, which were larger by up to a factor of 3 compared to the data assimilation at coarser resolutions. For tropospheric ozone, agreements with in situ ozone and ozonesonde observations were improved after data assimilation at 0.56° resolution compared to coarser resolutions. These results suggested that the data assimilation at 0.56° resolution can make better use of observational information than at coarser resolutions, because increasing horizontal resolution allowed the assimilation to improve spatial representativeness errors between assimilated observations and model simulations, to consider small-scale variations in background error covariance through nonlinear transport and chemical processes, and to capture the fine-scale features of the precursor emissions, particularly for the surface ozone analysis.

Using the ozonesonde measurements, the performance of the data assimilation at 0.56° resolution was comparable to the CAMS reanalysis for all latitude bands, as consistently reported in an inter-comparison study of several tropospheric ozone reanalysis products including TCR-2 and CAMS (Huijnen et al., 2019; Park et al., 2020). In the upper troposphere, mean biases and RMSEs for the data assimilation analysis at 0.56° resolution against ozonesonde observations were slightly larger than those for the MERRA-2 analysis.

6.2. Importance of Horizontal Resolution on Emission Estimation

As shown in Section 5.2, estimating NO_x emissions at the megacity scale (e.g., 0.56°) substantially influences domain total (i.e., 2.8°) emission estimates. Global total NO_x emission estimates at 0.56° resolution over areas with medium and strong sources were 15% smaller than those at coarser resolutions, with larger differences over megacities such as Los Angeles (by up to 41%) and Shanghai (by up to 17%). These results could be attributed to smaller domain-averaged OH concentration analysis over areas with strong sources such as Los Angeles (13%) and Shanghai (7%) at 0.56° resolution compared to those at 2.8° resolution, which is associated with suppressed instantaneous mixing in model grid cells and subsequent feedback from the ozone-HO_x-NO_x chemistry.

A 5–15 km resolution would be required to improve the chemical feedback as demonstrated in previous studies (Charlton-Perez et al., 2009; Valin et al., 2011) and to fully take advantage of high-resolution future satellite measurements (X. Liu et al., 2017). Thus, further improvements in NO_x emission estimates would be attainable using the data assimilation at a horizontal resolution finer than 0.56°.

6.3. Potential Contribution of Globally Consistent Information of Trace Gas Emissions and Concentrations on a Megacity Scale

Globally consistent data assimilation analysis would benefit studies on atmospheric environment such as evaluation of bottom-up emission estimates and health impact assessment of air pollutions. Updates on

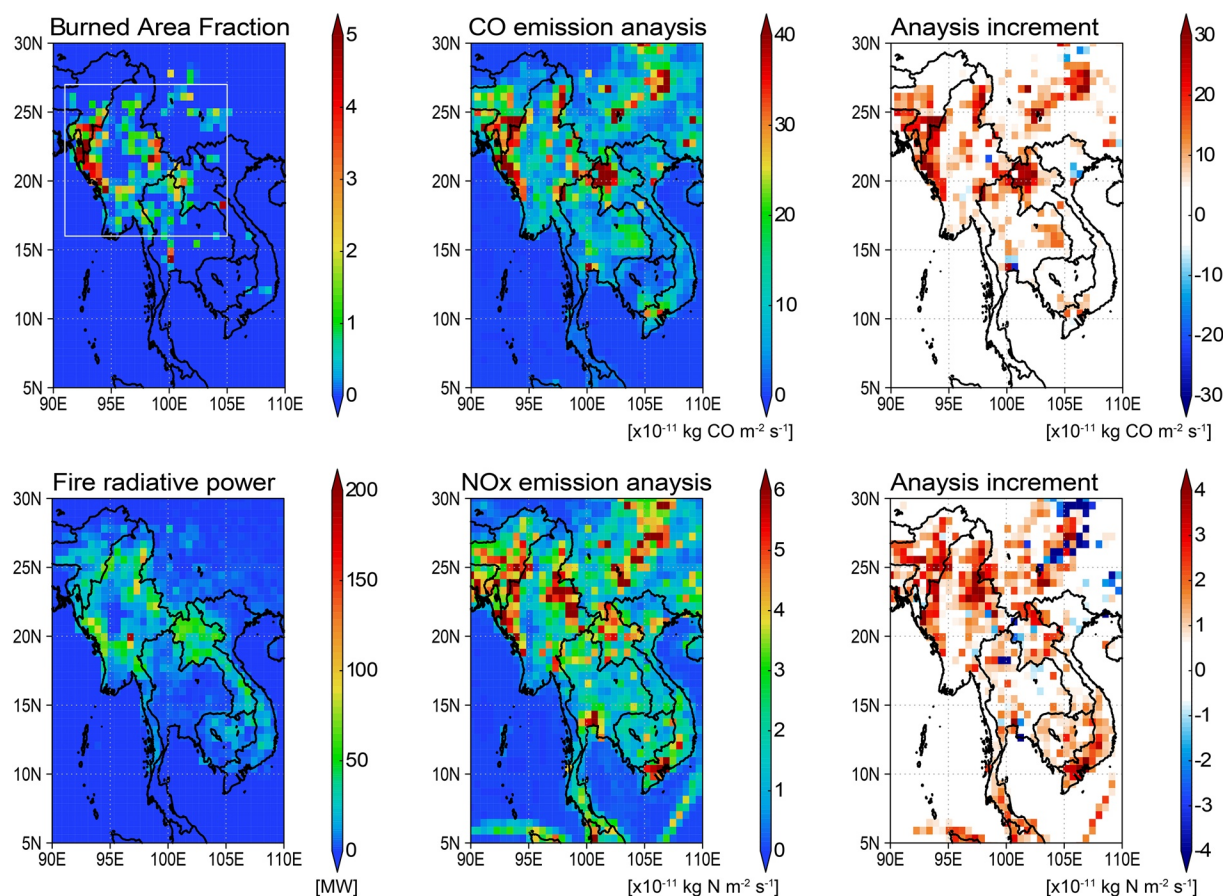


Figure 11. Regional distribution of burned area fraction (BAF), fire radiative power (FRP), and a posteriori CO and NO_x emissions and their analysis increments over Southeast Asia during April 8–30. The left column is the BAF (upper row) and FRP (bottom row). The middle and right columns are the a posteriori emissions and their analysis increments of CO (upper row) and NO_x (bottom row), respectively. The a posteriori emissions are derived from a 0.56°-resolution data assimilation with 64 ensembles. The units of FRP, CO, and NO_x emissions are MW, $\times 10^{-11}$ kg CO m⁻² s⁻¹, and $\times 10^{-11}$ kg N m⁻² s⁻¹, respectively.

various aspects (e.g., uncertainty, resolution) have also improved the bottom-up estimates for anthropogenic and biomass burning emissions (e.g., Crippa et al., 2018; van der Werf et al., 2017). Our analysis would provide complementary information on spatial and temporal variations in anthropogenic emission factors and activity rates over megacities for different regions of the world. More detailed analysis would be useful for improving bottom-up emission inventories, especially for developing countries where large uncertainty remains. For biomass burning emissions, data assimilation analysis can be used to study detailed spatio-temporal variations in emission factors. In this study, we assumed the fixed initial uncertainty in a priori emissions (i.e., 60%), because gridded uncertainties in emission inventories are not available. If the gridded uncertainties will be available like CO₂ emission inventories (e.g., Andres et al., 2016; Super et al., 2020), our data assimilation framework can account for uncertainties in a priori emissions more appropriately, which would support a verification of bottom-up emission estimates. Note that the CO emission estimates from this study will contain uncertainties because of the short-data assimilation window and the sparse observation coverage over the biomass burning areas.

A potential important application of the developed 0.56°-resolution data assimilation is health impact assessments of air pollution. This study demonstrates that data assimilation at 2.8° resolution overestimates the population-weighted ozone concentrations over polluted areas, compared to at 0.56° resolution, which suggests that the globally consistent information on a megacity scale obtained from the chemical data assimilation would help improve global-scale health impact assessments using CTMs (e.g., Liang et al., 2018), because observational information on ozone and its precursors is incorporated into the system. Regional

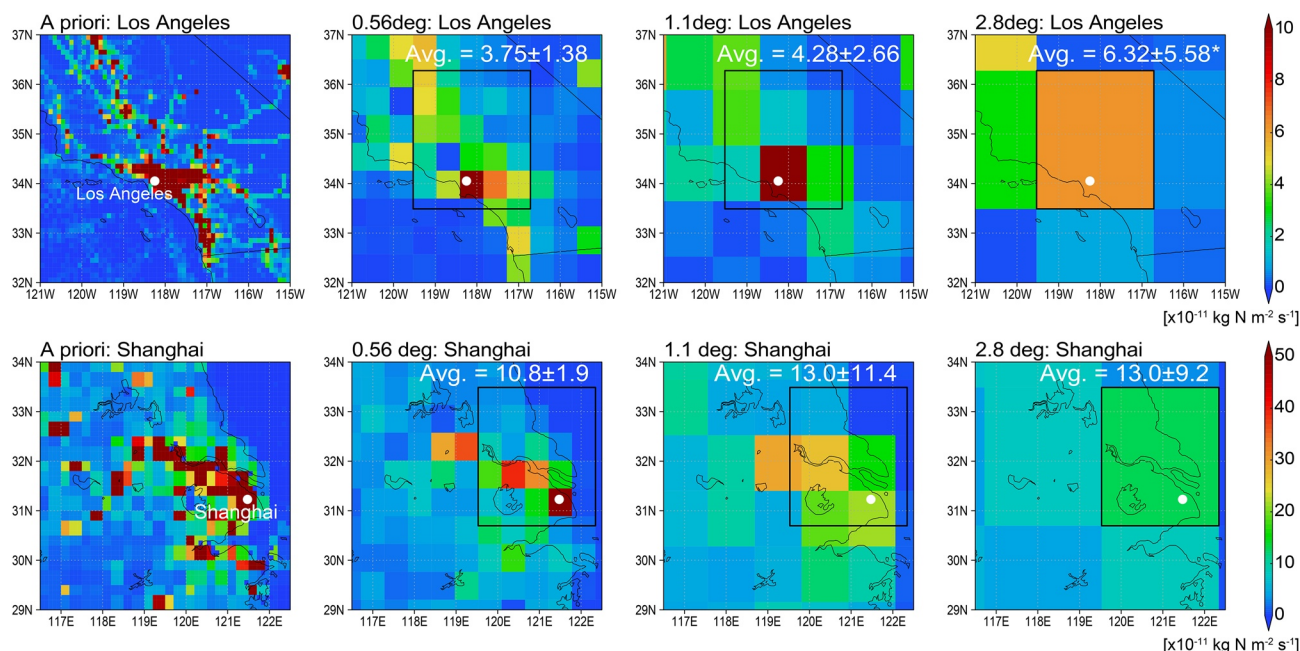


Figure 12. Spatial distribution of the a posteriori NO_x emission ($\times 10^{-11} \text{ kg N m}^{-2} \text{ s}^{-1}$) around Los Angeles (upper row) and Shanghai (lower row) derived from the HTAP_v2.2 bottom-up emission inventory (first column) and data assimilation with 32 ensembles at 0.56° (second column), 1.1° (third column), and 2.8° (fourth column) resolutions. The solid square is the 2.8° -bin grid that covers Los Angeles and Shanghai. “Avg.” means the average emission with analysis spread in the solid square. The asterisk indicates that difference of “Avg” from that at 0.56° resolution is statistically significant at the 95% confidence level using the two-sample *t*-test.

modeling framework at resolutions of 10 km or finer, such as the CAMS regional data sets (CAMS, 2020; Marécal et al., 2015), would be needed to study spatial and temporal variations in emissions and concentrations at an urban scale and their health impacts, as demonstrated in previous works (e.g., Barré et al., 2020; Russell et al., 2019; Thompson & Selin, 2012). Although a 0.56° resolution is coarser than these regional modeling studies, globally consistent analyses constructed in this study can characterize features at megacities over different regions of the world.

7. Summary and Conclusions

We conducted global data assimilation experiments at 0.56° resolution which integrates satellite measurements of multiple trace gases using the combination with the LETKF approach (Miyazaki, Sekiya, et al., 2019) and a 0.56° -resolution global CTM (Sekiya et al., 2018). This approach allows high-resolution satellite retrievals to be assimilated more efficiently and consistently, which is important for globally consistent analyses of emissions and concentrations on a megacity scale. Assimilated satellite retrievals of ozone, NO_2 , CO, HNO_3 , and SO_2 were obtained from multiple sensors (OMI, GOME-2, SCIAMACHY, TES, MOPITT, and MLS) during the boreal spring and summer of 2008. The data assimilation at 0.56° resolution reduced model biases of NO_2 and ozone concentrations against independent surface, ozonesonde, and aircraft observations, which was larger than that at coarser resolutions (1.1° and 2.8°) for many cases. It reduced model biases against surface NO_2 measurements by 33%–75% over major polluted regions and surface ozone by 18% and 15% over the United States and East Asia, respectively. Increasing model resolution from 2.8° to 0.56° resulted in larger error reductions against assimilated observations for NO_2 by factors of 1.5–3, especially for megacities in China such as Beijing, Shanghai, and Guangzhou. The remaining errors after data assimilation at 0.56° resolution were significantly smaller than at 2.8° resolution (by up to 35%).

The horizontal model resolution has substantial impact on surface NO_x emission estimates, depending on emission strength. The estimated emissions at 0.56° resolution were smaller by 15% on average than those at 2.8° resolution over medium and strong emission sources ($> 3 \times 10^{-11} \text{ kg N m}^{-2} \text{ s}^{-1}$), with larger differences over megacities such as Los Angeles (by -41%). Over weak sources ($< 3 \times 10^{-11} \text{ kg N m}^{-2} \text{ s}^{-1}$), mean

differences were statistically insignificant, except for 5%–7% smaller emission estimates at 0.56° resolution over ship lanes in the Pacific and Atlantic. The strong model resolution dependence of NO_x emission estimates can be associated with the impacts of horizontal resolution on NO_x lifetime determined by the nonlinear chemical and transport processes. Most bottom-up emission inventories have finer resolution than 0.56°, whereas they have large uncertainties in spatial and temporal emission variability. The 0.56°-resolution emission estimates constrained by observational information can be used to study the emission variability on a megacity scale.

The global chemical data assimilation experiments at 0.56, 1.1, and 2.8° resolutions demonstrate substantial impacts of increasing horizontal model resolution on agreements of NO₂ and ozone concentration analyses against independent observations and on surface NO_x emission estimates over different regions of the world. This framework is expected to provide fundamentally different information from combination of separated regional analysis system (e.g., Ding et al., 2015; X. Liu et al., 2017; Souri et al., 2016), which is suitable for evaluating region-by-region differences in megacity-scale air pollutions and their impact on human health. The global data assimilation system at 0.56° resolution will be a powerful tool to harness the potential of observational information from more advanced high-resolution low earth orbit satellite instruments (e.g., TROPOMI, IASI-NG, and CrIS) and future geostationary satellite instruments (e.g., Sentinel-4, TEMPO, and GEMS), which, in turn, will provide valuable information on long-term changes in atmospheric environment and its impact on human health on a megacity scale.

Data Availability Statement

The authors acknowledge the use of tropospheric NO₂ column data from OMI, GOME-2, and SCIAMACHY sensors from the Quality Assurance for Essential Climate Variables (QA4ECV) project (<http://www.qa4ecv.eu/>), the TES ozone, MLS ozone, HNO₃, MOPITT CO, MLS-TES CO and MODIS active fire products from the NASA Aura, EOS Terra, and Aqua satellites (<https://earthdata.nasa.gov/>), the surface NO₂ measurement data from EEA (<https://www.eea.europa.eu/>), US EPA (<https://www.epa.gov/aqs>), Hong Kong EPD (<https://www.epd.gov.hk/epd/>), and NIES (<http://www.nies.go.jp/>), ozonesonde data from the WOUDC (<https://woudc.org/>), SHADOZ (<https://tropo.gsfc.nasa.gov/shadoz/>), and the NOAA ESRL GMD (<https://www.esrl.noaa.gov/gmd/>), the surface ozone measurement data from EMEP (<http://ebas.nilu.no/>), CAST-NET (<https://www.epa.gov/castnet>), EANET (<http://www.eanet.asia/>), and WDCGG (<https://ds.data.jma.go.jp/gmd/wdcgg/>), the top-down NO_x emission data from DECSO obtained from the GlobEmission project (<http://www.globemission.eu>) and the GFED4 daily burned area data from the Global Fire Emission Database (<https://www.globalfiredata.org>). The Earth Simulator was used for data assimilation calculations with the support of the Japan Agency for Marine-Earth Science and Technology (as a JAMSTEC Proposed Project and Strategic Project with Special Support). Further, we referred to the 2008 ARCTAS campaign from the NASA LaRC Airborne Science Data for Atmospheric Composition. A part of the calculations were also conducted with the K computer provided by the RIKEN Advanced Institute for Computational Science through the HPCI System Research Project (Project ID: hp150288, hp160231, hp170232, and hp180181). The source code for the forecast model and data assimilation can be obtained from Kengo Sudo (kengo@nagoya-u.jp) and Kazuyuki Miyazaki (kazuyuki.miyazaki@jpl.nasa.gov) upon request, respectively. The 1.1°-resolution assimilation data are part of the TCR-2, which can be downloaded at <https://tes.jpl.nasa.gov/chemical-reanalysis/>. The 0.56°- and 2.8°-resolution assimilation data used in this manuscript are available online (https://figshare.com/projects/Sekiya_et_al_2020/79571).

Acknowledgments

This study was supported by the Post-K computer project Priority Issue 4 – Advancement of meteorological and global environmental predictions utilizing observational big data and by the Global Environment Research Fund (S-12) of the Ministry of the Environment (MOE). A part of the research was conducted at the Jet Propulsion Laboratory, California Institute of Technology, under a contract with the National Aeronautics and Space Administration.

References

- Akiyoshi, H., Nakamura, T., Miyasaka, T., Shiotani, M., & Suzuki, M. (2016). A nudged chemistry-climate model simulation of chemical constituent distribution at northern high-latitude stratosphere observed by smiles and mls during the 2009/2010 stratospheric sudden warming. *Journal of Geophysical Research - D: Atmospheres*, 121(3), 1361–1380. <https://doi.org/10.1002/2015JD023334>
- Akiyoshi, H., Zhou, L. B., Yamashita, Y., Sakamoto, K., Yoshiki, M., Nagashima, T., et al. (2009). A CCM simulation of the breakup of the Antarctic polar vortex in the years 1980–2004 under the CCMVal scenarios. *Journal of Geophysical Research*, 114(D3), D03103. <https://doi.org/10.1029/2007JD009261>
- Anderson, J. L. (2009). Spatially and temporally varying adaptive covariance inflation for ensemble filters. *Tellus A*, 61(1), 72–83. <https://doi.org/10.1111/j.1600-0870.2008.00361.x>
- Andres, R. J., Boden, T. A., & Higdon, D. M. (2016). Gridded uncertainty in fossil fuel carbon dioxide emission maps, a CDIAC example. *Atmospheric Chemistry and Physics*, 16(23), 14979–14995. <https://doi.org/10.5194/acp-16-14979-2016>

- Baklanov, A., Molina, L. T., & Gauss, M. (2016). Megacities, air quality and climate. *Atmospheric Environment*, 126, 235–249. <https://doi.org/10.1016/j.atmosenv.2015.11.059>
- Banerjee, A., Maycock, A. C., Archibald, A. T., Abraham, N. L., Telford, P., Braesicke, P., & Pyle, J. A. (2016). Drivers of changes in stratospheric and tropospheric ozone between year 2000 and 2100. *Atmospheric Chemistry and Physics*, 16(5), 2727–2746. <https://doi.org/10.5194/acp-16-2727-2016>
- Barré, J., Petetin, H., Colette, A., Guevara, M., Peuch, V.-H., Rouil, L., et al. (2020). Estimating lockdown induced European NO₂ changes. *Atmospheric Chemistry and Physics Discussions*, 1–28. <https://doi.org/10.5194/acp-2020-995>
- Bocquet, M., Elbern, H., Eskes, H., Hirtl, M., Žabkar, R., Carmichael, G. R., et al. (2015). Data assimilation in atmospheric chemistry models: Current status and future prospects for coupled chemistry meteorology models. *Atmospheric Chemistry and Physics*, 15(10), 5325–5358. <https://doi.org/10.5194/acp-15-5325-2015>
- Boersma, K. F., Eskes, H. J., Richter, A., De Smedt, I., Lorente, A., Beirle, S., et al. (2018). Improving algorithms and uncertainty estimates for satellite NO₂ retrievals: Results from the Quality Assurance for Essential Climate Variables (QA4ECV) project. *Atmospheric Measurement Techniques Discussions*, 1–70. <https://doi.org/10.5194/amt-2018-200>
- Boersma, K. F., Eskes, H., Richter, A., De Smedt, I., Lorente, A., Beirle, S., et al. (2017a). QA4ECV NO₂ tropospheric and stratospheric vertical column data from GOME-2A (Version 1.1). [Data set]. <https://doi.org/10.21944/qa4ecv-no2-gome2a-v1.1>
- Boersma, K. F., Eskes, H., Richter, A., De Smedt, I., Lorente, A., Beirle, S., et al. (2017b). QA4ECV NO₂ tropospheric and stratospheric vertical column data from OMI (Version 1.1). [Data set]. <https://doi.org/10.21944/qa4ecv-no2-omi-v1.1>
- Boersma, K. F., Eskes, H., Richter, A., De Smedt, I., Lorente, A., Beirle, S., et al. (2017c). QA4ECV NO₂ tropospheric and stratospheric vertical column data from SCIAMACHY (Version 1.1). [Data set]. <https://doi.org/10.21944/qa4ecv-no2-scia-v1.1>
- Boersma, K. F., Vinken, G. C. M., & Eskes, H. J. (2016). Representativeness errors in comparing chemistry transport and chemistry climate models with satellite UV-Vis tropospheric column retrievals. *Geoscientific Model Development*, 9(2), 875–898. <https://doi.org/10.5194/gmd-9-875-2016>
- Boersma, K. F., Vinken, G. C. M., & Tournadre, J. (2015). Ships going slow in reducing their NO_x emissions: Changes in 2005–2012 ship exhaust inferred from satellite measurements over Europe. *Environmental Research Letters*, 10(7), 074007. <https://doi.org/10.1088/1748-9326/10/7/074007>
- Boxe, C. S., Worden, J. R., Bowman, K. W., Kulawik, S. S., Neu, J. L., Ford, W. C., et al. (2010). Validation of northern latitude Tropospheric Emission Spectrometer stare ozone profiles with ARC-IONS sondes during ARCTAS: Sensitivity, bias and error analysis. *Atmospheric Chemistry and Physics*, 10(20), 9901–9914. <https://doi.org/10.5194/acp-10-9901-2010>
- Brasseur, G. P., & Jacob, D. J. (2017). *Modeling of atmospheric chemistry*. Cambridge University Press. <https://doi.org/10.1017/9781316544754>
- CAMS. (2020). *Regional air quality production systems*. Retrieved from <https://atmosphere.copernicus.eu/documentation-regional-systems>
- Cantrell, C. A., Edwards, G. D., Stephens, S., Mauldin, R. L., Zondlo, M. A., Kosciuch, E., et al. (2003). Peroxy radical behavior during the transport and chemical evolution over the pacific (TRACE-P) campaign as measured aboard the NASA P-3B aircraft. *Journal of Geophysical Research*, 108(D20). <https://doi.org/10.1029/2003JD003674>
- Castellanos, P., Boersma, K. F., & van der Werf, G. R. (2014). Satellite observations indicate substantial spatiotemporal variability in biomass burning NO_x emission factors for South America. *Atmospheric Chemistry and Physics*, 14(8), 3929–3943. <https://doi.org/10.5194/acp-14-3929-2014>
- Charlton-Perez, C. L., Evans, M. J., Marsham, J. H., & Esler, J. G. (2009). The impact of resolution on ship plume simulations with NO_x chemistry. *Atmospheric Chemistry and Physics*, 9(19), 7505–7518. <https://doi.org/10.5194/acp-9-7505-2009>
- Chatterjee, A., & Michalak, A. M. (2013). Technical Note: Comparison of ensemble Kalman filter and variational approaches for CO₂ data assimilation. *Atmospheric Chemistry and Physics*, 13(23), 11643–11660. <https://doi.org/10.5194/acp-13-11643-2013>
- CIESIN, C. U., & Center for International Earth Science Information Network. (2018). *Gridded population of the world, version 4 (GPWv4): Population density adjusted to match 2015 revision UN WPP country totals, revision 11*. NASA Socioeconomic Data and Applications Center (SEDAC). <https://doi.org/10.7927/H4F47M65>
- Crippa, M., Guizzardi, D., Muntean, M., Schaaf, E., Dentener, F., van Aardenne, J. A., et al. (2018). Gridded emissions of air pollutants for the period 1970–2012 within EDGAR v4.3.2. *Earth System Science Data*, 10(4), 1987–2013. <https://doi.org/10.5194/essd-10-1987-2018>
- Crounse, J. D., McKinney, K. A., Kwan, A. J., & Wennberg, P. O. (2006). Measurement of gas-phase hydroperoxides by chemical ionization mass spectrometry. *Analytical Chemistry*, 78(19), 6726–6732. <https://doi.org/10.1021/ac0604235>
- Dee, D. P., Uppala, S. M., Simmons, A. J., Berrisford, P., Poli, P., Kobayashi, S., et al. (2011). The ERA-Interim reanalysis: Configuration and performance of the data assimilation system. *Quarterly Journal of the Royal Meteorological Society*, 137(656), 553–597. <https://doi.org/10.1002/qj.828>
- Deeter, M. N., Edwards, D. P., Francis, G. L., Gille, J. C., Martínez-Alonso, S., Worden, H. M., & Sweeney, C. (2017). A climate-scale satellite record for carbon monoxide: The MOPITT version 7 product. *Atmospheric Measurement Techniques*, 10(7), 2533–2555. <https://doi.org/10.5194/amt-10-2533-2017>
- Ding, J., van der A, R. J., Mijling, B., Jalkanen, J.-P., Johansson, L., & Levelt, P. F. (2018). Maritime NO_x emissions over Chinese seas derived from satellite observations. *Geophysical Research Letters*, 45(4), 2031–2037. <https://doi.org/10.1002/2017GL076788>
- Ding, J., van der A, R. J., Mijling, B., Levelt, P. F., & Hao, N. (2015). NO_x emission estimates during the 2014 Youth Olympic Games in Nanjing. *Atmospheric Chemistry and Physics*, 15(16), 9399–9412. <https://doi.org/10.5194/acp-15-9399-2015>
- Eastham, S. D., & Jacob, D. J. (2017). Limits on the ability of global Eulerian models to resolve intercontinental transport of chemical plumes. *Atmospheric Chemistry and Physics*, 17(4), 2543–2553. <https://doi.org/10.5194/acp-17-2543-2017>
- Elguindi, N., Granier, C., Stavrou, T., Darras, S., Bauwens, M., Cao, H., et al. (2020). Intercomparison of magnitudes and trends in anthropogenic surface emissions from bottom-up inventories, top-down estimates, and emission scenarios. *Earth's Future*, 8(8), e2020EF001520. <https://doi.org/10.1029/2020EF001520>
- Emori, S., Nozawa, T., Numaguti, A., & Uno, I. (2001). Importance of cumulus parameterization for precipitation simulation over east Asia in June. *Journal of the Meteorological Society of Japan*, 79(4), 939–947. <https://doi.org/10.2151/jmsj.79.939>
- Eskes, H. J., Velthoven, P. F. J. V., Valks, P. J. M., & Kelder, H. M. (2003). Assimilation of GOME total-ozone satellite observations in a three-dimensional tracer-transport model. *Quarterly Journal of the Royal Meteorological Society*, 129(590), 1663–1681. <https://doi.org/10.1256/qj.02.14>
- Evensen, G. (2009). The ensemble Kalman filter for combined state and parameter estimation. *IEEE Control Systems*, 29(3), 83–104. <https://doi.org/10.1109/mcs.2009.932223>
- Fertig, E. J., Harlim, J., & Hunt, B. R. (2007). A comparative study of 4D-VAR and a 4D ensemble Kalman filter: Perfect model simulations with Lorenz-96. *Tellus A: Dynamic Meteorology and Oceanography*, 59(1), 96–100. <https://doi.org/10.1111/j.1600-0870.2006.00205.x>

- Fioletov, V. E., McLinden, C. A., Krotkov, N., Li, C., Joiner, J., Theys, N., et al. (2016). A global catalog of large SO₂ sources and emissions derived from the Ozone Monitoring Instrument. *Atmospheric Chemistry and Physics*, 16(18), 11497–11519. <https://doi.org/10.5194/acp-16-11497-2016>
- Fioletov, V., McLinden, C. A., Kharol, S. K., Krotkov, N. A., Li, C., Joiner, J., et al. (2017). Multi-source SO₂ emission retrievals and consistency of satellite and surface measurements with reported emissions. *Atmospheric Chemistry and Physics*, 17(20), 12597–12616. <https://doi.org/10.5194/acp-17-12597-2017>
- Giglio, L. (2015). *MODIS collection 6 active fire product user's guide revision A*. (Unpublished Manuscript). Department of Geographical Sciences, University of Maryland. Retrieved from https://lpdaac.usgs.gov/sites/default/files/public/product_documentation/mod14_user_guide.pdf
- Giglio, L., Randerson, J. T., & van der Werf, G. R. (2013). Analysis of daily, monthly, and annual burned area using the fourth-generation global fire emissions database (GFED4). *Journal of Geophysical Research: Biogeosciences*, 118(1), 317–328. <https://doi.org/10.1002/jgrg.20042>
- Gluck, S., Glenn, C., Logan, T., Vu, B., Walsh, M., & Williams, P. (2003). Evaluation of NO_x flue gas analyzers for accuracy and their applicability for low-concentration measurements. *Journal of the Air & Waste Management Association*, 53(6), 749–758. <https://doi.org/10.1080/10473289.2003.10466208>
- Herman, R. L., & Kulawik, S. S. (Eds.). (2013). *Tropospheric Emission Spectrometer TES Level 2 (L2) Data User's Guide (Final) (No. Version 5.0 JPL D-38042)*. Jet Propulsion Laboratory, California Institute of Technology. Retrieved from <https://eosweb.larc.nasa.gov/project/tes/validation>
- Hudman, R. C., Moore, N. E., Mebust, A. K., Martin, R. V., Russell, A. R., Valin, L. C., & Cohen, R. C. (2012). Steps toward a mechanistic model of global soil nitric oxide emissions: Implementation and space based-constraints. *Atmospheric Chemistry and Physics*, 12(16), 7779–7795. <https://doi.org/10.5194/acp-12-7779-2012>
- Huijnen, V., Eskes, H. J., Poupkou, A., Elbern, H., Boersma, K. F., Foret, G., et al. (2010). Comparison of OMI NO₂ tropospheric columns with an ensemble of global and European regional air quality models. *Atmospheric Chemistry and Physics*, 10(7), 3273–3296. <https://doi.org/10.5194/acp-10-3273-2010>
- Huijnen, V., Miyazaki, K., Flemming, J., Inness, A., Sekiya, T., & Schultz, M. G. (2019). An inter-comparison of CAMS and TCR tropospheric ozone reanalysis products. *Atmospheric Chemistry and Physics*, 13(3), 1513–1544.
- Hunt, B. R., Kostelich, E. J., & Szunyogh, I. (2007). Efficient data assimilation for spatiotemporal chaos: A local ensemble transform Kalman filter. *Physica D: Nonlinear Phenomena*, 230(1), 112–126. <https://doi.org/10.1016/j.physd.2006.11.008>
- Inness, A., Ades, M., Agustí-Panareda, A., Barré, J., Benedictow, A., Blechschmidt, A.-M., et al. (2019). The CAMS reanalysis of atmospheric composition. *Atmospheric Chemistry and Physics*, 19(6), 3515–3556. <https://doi.org/10.5194/acp-19-3515-2019>
- IPCC. (2013). *Climate change 2013: The physical science basis. Contribution of working group I to the fifth assessment report of the intergovernmental panel on climate change*. Cambridge University Press. <https://doi.org/10.1017/CBO9781107415324>
- Jacob, D. J., Crawford, J. H., Maring, H., Clarke, A. D., Dibb, J. E., Emmons, L. K., et al. (2010). The arctic research of the composition of the troposphere from aircraft and satellites (ARCTAS) mission: Design, execution, and first results. *Atmospheric Chemistry and Physics*, 10(11), 5191–5212. <https://doi.org/10.5194/acp-10-5191-2010>
- Jaeglé, L., Steinberger, L., Martin, R. V., & Chance, K. (2005). Global partitioning of NO_x sources using satellite observations: Relative roles of fossil fuel combustion, biomass burning and soil emissions. *Faraday Discussions*, 130, 407–423. <https://doi.org/10.1039/B502128F>
- Janssens-Maenhout, G., Crippa, M., Guizzardi, D., Dentener, F., Muntean, M., Pouliot, G., et al. (2015). HTAP_v2.2: A mosaic of regional and global emission grid maps for 2008 and 2010 to study hemispheric transport of air pollution. *Atmospheric Chemistry and Physics*, 15(19), 11411–11432. <https://doi.org/10.5194/acp-15-11411-2015>
- K-1 Model Developers. (2004). *K-1 coupled GCM (MIROC) description*. (Tech. Rep.). Center for Climate System Research (Univ. of Tokyo). National Institute for Environmental Studies, and Frontier Research Center for Global Change. Retrieved from http://ccsr.aori.u-tokyo.ac.jp/~hasumi/miroc_description.pdf
- Kalnay, E., Li, H., Miyoshi, T., Yang, S.-C., & Ballabrera-Poy, J. (2007). 4-D-Var or ensemble Kalman filter? *Tellus A: Dynamic Meteorology and Oceanography*, 59(5), 758–773. <https://doi.org/10.1111/j.1600-0870.2007.00261.x>
- Karambelas, A., Holloway, T., Kieseewetter, G., & Heyes, C. (2018). Constraining the uncertainty in emissions over India with a regional air quality model evaluation. *Atmospheric Environment*, 174, 194–203. <https://doi.org/10.1016/j.atmosenv.2017.11.052>
- Kim, S., Huey, L. G., Stickel, R. E., Tanner, D. J., Crawford, J. H., Olson, J. R., et al. (2007). Measurement of HO₂ NO₂ in the free troposphere during the Intercontinental Chemical Transport Experiment-North America 2004. *Journal of Geophysical Research*, 112(D12). <https://doi.org/10.1029/2006JD007676>
- Klich, C. A., & Fuelberg, H. E. (2014). The role of horizontal model resolution in assessing the transport of CO in a middle latitude cyclone using WRF-Chem. *Atmospheric Chemistry and Physics*, 14(2), 609–627. <https://doi.org/10.5194/acp-14-609-2014>
- Krotkov, N. A. (2012). *OMI/Aura Sulfur dioxide (SO₂) total column 1-orbit L2 swath 13×24 km*. NASA Goddard Earth Sciences Data and Information Services Center. <http://doi.org/10.5067/AURA/OMI/DATA2022>
- Lamsal, L. N., Martin, R. V., Padmanabhan, A., van Donkelaar, A., Zhang, Q., Sioris, C. E., et al. (2011). Application of satellite observations for timely updates to global anthropogenic NO_x emission inventories. *Geophysical Research Letters*, 38(5), L05810. <https://doi.org/10.1029/2010GL046476>
- Lamsal, L. N., Martin, R. V., Parrish, D. D., & Krotkov, N. A. (2013). Scaling relationship for NO₂ pollution and urban population size: A satellite perspective. *Environmental Science & Technology*, 47(14), 7855–7861. <https://doi.org/10.1021/es400744g>
- Lamsal, L. N., Martin, R. V., van Donkelaar, A., Steinbacher, M., Celarier, E. A., Bucsela, E., et al. (2008). Ground-level nitrogen dioxide concentrations inferred from the satellite-borne ozone monitoring instrument. *Journal of Geophysical Research*, 113(D16). <https://doi.org/10.1029/2007JD009235>
- Liang, C.-K., West, J. J., Silva, R. A., Bian, H., Chin, M., Davila, Y., et al. (2018). HTAP2 multi-model estimates of premature human mortality due to intercontinental transport of air pollution and emission sectors. *Atmospheric Chemistry and Physics*, 18(14), 10497–10520. <https://doi.org/10.5194/acp-18-10497-2018>
- Li, C., Joiner, J., Krotkov, N. A., & Bhartia, P. K. (2013). A fast and sensitive new satellite SO₂ retrieval algorithm based on principal component analysis: Application to the ozone monitoring instrument. *Geophysical Research Letters*, 40(23), 6314–6318. <https://doi.org/10.1002/2013GL058134>
- Lin, J.-T., McElroy, M. B., & Boersma, K. F. (2010). Constraint of anthropogenic NO_x emissions in China from different sectors: A new methodology using multiple satellite retrievals. *Atmospheric Chemistry and Physics*, 10(1), 63–78. <https://doi.org/10.5194/acp-10-63-2010>

- Lin, M., Fiore, A. M., Cooper, O. R., Horowitz, L. W., Langford, A. O., Levy, H., et al. (2012). Springtime high surface ozone events over the western United States: Quantifying the role of stratospheric intrusions. *Journal of Geophysical Research*, 117(D21). <https://doi.org/10.1029/2012JD018151>
- Liu, F., van der A, R. J., Eskes, H., Ding, J., & Mijling, B. (2018). Evaluation of modeling NO₂ concentrations driven by satellite-derived and bottom-up emission inventories using in situ measurements over China. *Atmospheric Chemistry and Physics*, 18(6), 4171–4186. <https://doi.org/10.5194/acp-18-4171-2018>
- Liu, X., Mizzi, A. P., Anderson, J. L., Fung, I. Y., & Cohen, R. C. (2017). Assimilation of satellite NO₂ observations at high spatial resolution using OSSEs. *Atmospheric Chemistry and Physics*, 17(11), 7067–7081. <https://doi.org/10.5194/acp-17-7067-2017>
- Livesey, N. J., Read, W. G., Froidevaux, L., Lambert, A., Manney, G. L., Pumphrey, H. C., et al. (2011). *Aura Microwave Limb Sounder (MLS), Version 3.3 Level 2 data quality and description document* (No. Tech. Rep. JPL D-33509). Jet Propulsion Laboratory. Retrieved from https://mls.jpl.nasa.gov/data/v3-3_data_quality_document.pdf
- Lu, Z., & Streets, D. G. (2012). Increase in NO_x emissions from Indian thermal power plants during 1996–2010: Unit-based inventories and multisatellite observations. *Environmental Science & Technology*, 46(14), 7463–7470. <https://doi.org/10.1021/es300831w>
- Manney, G. (2015). *MLS/Aura L2 nitric Acid (HNO₃) mixing ratio - version 4*. NASA Goddard Earth Sciences Data and Information Services Center. <http://doi.org/10.5067/AURA/MLS/DATA2012>
- Marécal, V., Peuch, V.-H., Andersson, C., Andersson, S., Arteta, J., Beekmann, M., & Ung, A. (2015). A regional air quality forecasting system over Europe: The MACC-II daily ensemble production. *Geoscientific Model Development*, 8(9), 2777–2813. <https://doi.org/10.5194/gmd-8-2777-2015>
- Mebust, A. K., & Cohen, R. C. (2014). Space-based observations of fire NO_x emission coefficients: A global biome-scale comparison. *Atmospheric Chemistry and Physics*, 14(5), 2509–2524. <https://doi.org/10.5194/acp-14-2509-2014>
- Ménard, R., & Chang, L.-P. (2000). Assimilation of stratospheric chemical tracer observations using a Kalman filter. Part II: χ^2 -validated results and analysis of variance and correlation dynamics. *Monthly Weather Review*, 128(8), 2672–2686. [https://doi.org/10.1175/1520-0493\(2000\)128<2672:AOSCTO>2.0.CO;2](https://doi.org/10.1175/1520-0493(2000)128<2672:AOSCTO>2.0.CO;2)
- Meul, S., Langematz, U., Kröger, P., Oberländer-Hayn, S., & Jöckel, P. (2018). Future changes in the stratosphere-to-troposphere ozone mass flux and the contribution from climate change and ozone recovery. *Atmospheric Chemistry and Physics*, 18(10), 7721–7738. <https://doi.org/10.5194/acp-18-7721-2018>
- Miyazaki, K., Bowman, K., Sekiya, T., Eskes, H., Boersma, F., Worden, H., et al. (2019). *Chemical reanalysis products*. NASA. Retrieved from <https://tes.jpl.nasa.gov/chemical-reanalysis/products/monthly-mean>
- Miyazaki, K., Bowman, K., Sekiya, T., Eskes, H., Boersma, F., Worden, H., et al. (2020). An updated tropospheric chemistry reanalysis and emission estimates, TCR-2, for 2005–2018. *Earth System Science Data Discussions*, 1–64. <https://doi.org/10.5194/essd-2020-30>
- Miyazaki, K., Bowman, K. W., Yumimoto, K., Walker, T., & Sudo, K. (2020). Evaluation of a multi-model, multi-constituent assimilation framework for tropospheric chemical reanalysis. *Atmospheric Chemistry and Physics*, 20(2), 931–967. <https://doi.org/10.5194/acp-20-931-2020>
- Miyazaki, K., & Eskes, H. (2013). Constraints on surface nox emissions by assimilating satellite observations of multiple species. *Geophysical Research Letters*, 40(17), 4745–4750. <https://doi.org/10.1002/grl.50894>
- Miyazaki, K., Eskes, H. J., & Sudo, K. (2012). Global NO_x emission estimates derived from an assimilation of OMI tropospheric NO₂ columns. *Atmospheric Chemistry and Physics*, 12(5), 2263–2288. <https://doi.org/10.5194/acp-12-2263-2012>
- Miyazaki, K., Eskes, H. J., & Sudo, K. (2015). A tropospheric chemistry reanalysis for the years 2005–2012 based on an assimilation of OMI, MLS, TES, and MOPITT satellite data. *Atmospheric Chemistry and Physics*, 15(14), 8315–8348. <https://doi.org/10.5194/acp-15-8315-2015>
- Miyazaki, K., Eskes, H. J., Sudo, K., Takigawa, M., van Weele, M., & Boersma, K. F. (2012). Simultaneous assimilation of satellite NO₂, O₃, CO, and HNO₃ data for the analysis of tropospheric chemical composition and emissions. *Atmospheric Chemistry and Physics*, 12(20), 9545–9579. <https://doi.org/10.5194/acp-12-9545-2012>
- Miyazaki, K., Eskes, H. J., Sudo, K., & Zhang, C. (2014). Global lightning NO_x production estimated by an assimilation of multiple satellite data sets. *Atmospheric Chemistry and Physics*, 14(7), 3277–3305. <https://doi.org/10.5194/acp-14-3277-2014>
- Miyazaki, K., Eskes, H., Sudo, K., Boersma, K. F., Bowman, K., & Kanaya, Y. (2017). Decadal changes in global surface NO_x emissions from multi-constituent satellite data assimilation. *Atmospheric Chemistry and Physics*, 17(2), 807–837. <https://doi.org/10.5194/acp-17-807-2017>
- Miyazaki, K., Sekiya, T., Fu, D., Bowman, K. W., Kulawik, S. S., Sudo, K., et al. (2019). Balance of emission and dynamical controls on ozone during the Korea–United States air quality campaign from multiconstituent satellite data assimilation. *Journal of Geophysical Research*, 124(1), 387–413. <https://doi.org/10.1029/2018JD028912>
- Miyoshi, T. (2011). The Gaussian approach to adaptive covariance inflation and its implementation with the local ensemble transform Kalman filter. *Monthly Weather Review*, 139(5), 1519–1535. <https://doi.org/10.1175/2010MWR3570.1>
- Morgenstern, O., Hegglin, M. I., Rozanov, E., O'Connor, F. M., Abraham, N. L., Akiyoshi, H., & Zeng, G. (2016). Review of the global models used within the chemistry-climate model initiative (CCMI). *Geoscientific Model Development Discussions*, 1–49. <https://doi.org/10.5194/gmd-2016-199>
- National Bureau of Statistics. (2018). *China statistical yearbook (2017)*. China Statistics Press. Retrieved from <http://www.stats.gov.cn/tjsj/ndsj/2017/indexeh.htm>
- National Capital Region Planning Board, G. o. I., Ministry of Urban Development. (2016). *Functional plan on drainage for national capital region*. Retrieved from http://ncrpb.nic.in/pdf_files/FP/%20on/%20Drainage/Chapter%201-%20-%20INTRODUCTION.pdf
- OECD. (2012). *Redefining urban: A new way to measure metropolitan areas*. Retrieved from <https://stats.oecd.org>
- Oikawa, P. Y., Ge, C., Wang, J., Eberwein, J. R., Liang, L. L., Allsman, L. A., & Jenerette, G. D. (2015). Unusually high soil nitrogen oxide emissions influence air quality in a high-temperature agricultural region. *Nature Communications*, 6, 8753. <https://doi.org/10.1038/ncomms9753>
- Park, S., Son, S.-W., Jung, M.-I., Park, J., & Park, S. S. (2020). Evaluation of tropospheric ozone reanalyses with independent ozonesonde observations in East Asia. *Geoscience Letters*, 7(1), 12. <https://doi.org/10.1186/s40562-020-00161-9>
- Prather, M. J., Zhu, X., Strahan, S. E., Steenrod, S. D., & Rodriguez, J. M. (2008). Quantifying errors in trace species transport modeling. *Proceedings of the National Academy of Sciences of the United States of America*, 105(50), 19617–19621. <https://doi.org/10.1073/pnas.0806541106>
- Price, C., & Rind, D. (1992). A simple lightning parameterization for calculating global lightning distributions. *Journal of Geophysical Research*, 97(D9), 9919–9933. <https://doi.org/10.1029/92JD00719>
- Qu, Z., Henze, D. K., Theyes, N., Wang, J., & Wang, W. (2019). Hybrid mass balance/4D-Var joint inversion of NO_x and SO₂ emissions in east Asia. *Journal of Geophysical Research*, 124(14), 8203–8224. <https://doi.org/10.1029/2018JD030240>

- Randerson, J. T., van der Werf, G. R., Giglio, L., Collatz, G. J., & Kasibhatla, P. S. (2018). *Global fire emissions database*. Version 4.1 (GFEDv4). ORNL Distributed Active Archive Center. Retrieved from https://daac.ornl.gov/cgi-bin/dsviewer.pl?ds_id=1293
- Russell, M., Hakami, A., Makar, P. A., Akingunola, A., Zhang, J., Moran, M. D., & Zheng, Q. (2019). An evaluation of the efficacy of very high resolution air-quality modeling over the Athabasca oil sands region, Alberta, Canada. *Atmospheric Chemistry and Physics*, 19(7), 4393–4417. <https://doi.org/10.5194/acp-19-4393-2019>
- Schwartz, M. (2015). *MLS/Aura L2 ozone (O3) mixing ratio – Version 4*. NASA Goddard Earth Sciences Data and Information Services Center. <http://doi.org/10.5067/AURA/MLS/DATA2017>
- Sekiya, T., Miyazaki, K., Ogochi, K., Sudo, K., & Takigawa, M. (2018). Global high-resolution simulations of tropospheric nitrogen dioxide using chaser v4.0. *Geoscientific Model Development*, 11(3), 959–988. <https://doi.org/10.5194/gmd-11-959-2018>
- Shindell, D. T., Faluvegi, G., Koch, D. M., Schmidt, G. A., Unger, N., & Bauer, S. E. (2009). Improved attribution of climate forcing to emissions. *Science*, 326(5953), 716–718. <https://doi.org/10.1126/science.1174760>
- Simpson, I. J., Akagi, S. K., Barletta, B., Blake, N. J., Choi, Y., Diskin, G. S., & Blake, D. R. (2011). Boreal forest fire emissions in fresh Canadian smoke plumes: C₁–C₁₀ volatile organic compounds (VOCs), CO₂, CO, NO₂, NO, HCN and CH₃CN. *Atmospheric Chemistry and Physics*, 11(13), 6445–6463. <https://doi.org/10.5194/acp-11-6445-2011>
- Skachko, S., Ménard, R., Errera, Q., Christophe, Y., & Chabrilat, S. (2016). EnKF and 4D-Var data assimilation with chemical transport model BASCOE (version 05.06). *Geoscientific Model Development*, 9(8), 2893–2908. <https://doi.org/10.5194/gmd-9-2893-2016>
- Souri, A. H., Choi, Y., Jeon, W., Li, X., Pan, S., Diao, L., & Westenbarger, D. A. (2016). Constraining NO_x emissions using satellite NO₂ measurements during 2013 DISCOVER-AQ Texas campaign. *Atmospheric Environment*, 131, 371–381. <https://doi.org/10.1016/j.atmosenv.2016.02.020>
- Souri, A. H., Choi, Y., Pan, S., Curci, G., Nowlan, C. R., Janz, S. J., & Weinheimer, A. J. (2018). First top-down estimates of anthropogenic NO_x emissions using high-resolution airborne remote sensing observations. *Journal of Geophysical Research*, 123(6), 3269–3284. <https://doi.org/10.1002/2017JD028009>
- Stavrakou, T., Müller, J.-F., Boersma, K. F., van der A, R. J., Kurokawa, J., Ohara, T., & Zhang, Q. (2013). Key chemical NO_x sink uncertainties and how they influence top-down emissions of nitrogen oxides. *Atmospheric Chemistry and Physics*, 13(17), 9057–9082. <https://doi.org/10.5194/acp-13-9057-2013>
- Sterling, C. W., Johnson, B. J., Oltmans, S. J., Smit, H. G. J., Jordan, A. F., Cullis, P. D., & Witte, J. C. (2018). Homogenizing and estimating the uncertainty in NOAA's long-term vertical ozone profile records measured with the electrochemical concentration cell ozonesonde. *Atmospheric Measurement Techniques*, 11(6), 3661–3687. <https://doi.org/10.5194/amt-11-3661-2018>
- Stock, Z. S., Russo, M. R., & Pyle, J. A. (2014). Representing ozone extremes in European megacities: The importance of resolution in a global chemistry climate model. *Atmospheric Chemistry and Physics*, 14(8), 3899–3912. <https://doi.org/10.5194/acp-14-3899-2014>
- Streets, D. G., Bond, T. C., Carmichael, G. R., Fernandes, S. D., Fu, Q., He, D., & Yarber, K. F. (2003). An inventory of gaseous and primary aerosol emissions in Asia in the year 2000. *Journal of Geophysical Research*, 108(D21). <https://doi.org/10.1029/2002JD003093>
- Streets, D. G., Canty, T., Carmichael, G. R., de Foy, B., Dickerson, R. R., Duncan, B. N., & Wecht, K. J. (2013). Emissions estimation from satellite retrievals: A review of current capability. *Atmospheric Environment*, 77, 1011–1042. <https://doi.org/10.1016/j.atmosenv.2013.05.051>
- Sudo, K., Takahashi, M., Kurokawa, J., & Akimoto, H. (2002). CHASER: A global chemical model of the troposphere 1. Model description. *Journal of Geophysical Research*, 107(D17), ACH 7-1–ACH 7-20. <https://doi.org/10.1029/2001JD001113>
- Super, I., Dellaert, S. N. C., Visschedijk, A. J. H., & Denier van der Gon, H. A. C. (2020). Uncertainty analysis of a European high-resolution emission inventory of CO₂ and CO to support inverse modeling and network design. *Atmospheric Chemistry and Physics*, 20(3), 1795–1816. <https://doi.org/10.5194/acp-20-1795-2020>
- Tao, Z., Chin, M., Gao, M., Kucsera, T., Kim, D., Bian, H., & Akimoto, H. (2020). Evaluation of NU-WRF model performance on air quality simulation under various model resolutions – An investigation within the framework of MICS-Asia Phase III. *Atmospheric Chemistry and Physics*, 20(4), 2319–2339. <https://doi.org/10.5194/acp-20-2319-2020>
- TES Science Team. (2017). *TES/Aura L2 ozone Nadir – version 7*. NASA Langley Atmospheric Science Data Center DAAC. Retrieved from https://asdc.larc.nasa.gov/project/TES/TL2O3N_7
- The United Nations, P. D., Department of Economic and Social Affairs. (2015). *World Urbanization Prospects: The 2014 revision*. Retrieved from <https://population.un.org/wup/Publications/Files/WUP2014-Report.pdf>
- Thompson, A. M., Witte, J. C., Sterling, C., Jordan, A., Johnson, B. J., Oltmans, S. J., & Thiongo, K. (2017). First reprocessing of southern hemisphere additional ozonesondes (shadoz) ozone profiles (1998–2016): 2. Comparisons with satellites and ground-based instruments. *Journal of Geophysical Research*, 122(23), 13000–13025. <https://doi.org/10.1002/2017JD027406>
- Thompson, T. M., & Selin, N. E. (2012). Influence of air quality model resolution on uncertainty associated with health impacts. *Atmospheric Chemistry and Physics*, 12(20), 9753–9762. <https://doi.org/10.5194/acp-12-9753-2012>
- Tie, X., Brasseur, G., & Ying, Z. (2010). Impact of model resolution on chemical ozone formation in Mexico City: Application of the WRF-Chem model. *Atmospheric Chemistry and Physics*, 10(18), 8983–8995. <https://doi.org/10.5194/acp-10-8983-2010>
- Valari, M., & Menut, L. (2008). Does an increase in air quality models' resolution bring surface ozone concentrations closer to reality? *Journal of Atmospheric and Oceanic Technology*, 25(11), 1955–1968. <https://doi.org/10.1175/2008JTECHA1123.1>
- Valin, L. C., Russell, A. R., Hudman, R. C., & Cohen, R. C. (2011). Effects of model resolution on the interpretation of satellite NO₂ observations. *Atmospheric Chemistry and Physics*, 11(22), 11647–11655. <https://doi.org/10.5194/acp-11-11647-2011>
- van der Werf, G. R., Randerson, J. T., Giglio, L., van Leeuwen, T. T., Chen, Y., Rogers, B. M., & Kasibhatla, P. S. (2017). Global fire emissions estimates during 1997–2016. *Earth System Science Data*, 9(2), 697–720. <https://doi.org/10.5194/essd-9-697-2017>
- Vinken, G. C. M., Boersma, K. F., Maasakkers, J. D., Adon, M., & Martin, R. V. (2014). World wide biogenic soil NO_x emissions inferred from OMI NO₂ observations. *Atmospheric Chemistry and Physics*, 14(18), 10363–10381. <https://doi.org/10.5194/acp-14-10363-2014>
- Watanabe, S., Hajima, T., Sudo, K., Nagashima, T., Takemura, T., Okajima, H., & Kawamiya, M. (2011). MIROC-ESM 2010: Model description and basic results of CMIP5-20c3m experiments. *Geoscientific Model Development*, 4(4), 845–872. <https://doi.org/10.5194/gmd-4-845-2011>
- Weber, B., Wu, D., Tamm, A., Ruckteschler, N., Rodríguez-Caballero, E., Steinkamp, J., & Pöschl, U. (2015). Biological soil crusts accelerate the nitrogen cycle through large NO and HONO emissions in drylands. *Proceedings of the National Academy of Sciences of the United States of America*, 112(50), 15384–15389. <https://doi.org/10.1073/pnas.1515818112>
- Weinheimer, A. J., Walega, J. G., Ridley, B. A., Gary, B. L., Blake, D. R., Blake, N. J., & Collins, J. E. (1994). Meridional distributions of NO_x, NO_y, and other species in the lower stratosphere and upper troposphere during AASE II. *Geophysical Research Letters*, 21(23), 2583–2586. <https://doi.org/10.1029/94GL01897>
- WHO, W. H. O. (2016). *Ambient air pollution: A global assessment of exposure and burden of disease*. The WHO document production services. Retrieved from <https://apps.who.int/iris/bitstream/handle/10665/250141/9789241511353-eng.pdf>

- Wild, O., & Prather, M. J. (2006). Global tropospheric ozone modeling: Quantifying errors due to grid resolution. *Journal of Geophysical Research*, 111(D11), D11305. <https://doi.org/10.1029/2005JD006605>
- Williams, J. E., Boersma, K. F., Le Sager, P., & Verstraeten, W. W. (2017). The high-resolution version of TM5-MP for optimized satellite retrievals: Description and validation. *Geoscientific Model Development*, 10(2), 721–750. <https://doi.org/10.5194/gmd-10-721-2017>
- Witte, J. C., Thompson, A. M., Smit, H. G. J., Fujiwara, M., Posny, F., Coetzee, G. J. R., & da Silva, F. R. (2017). First reprocessing of southern hemisphere additional ozonesondes (shadoz) profile records (1998–2015): 1. Methodology and evaluation. *Journal of Geophysical Research*, 122(12), 6611–6636. <https://doi.org/10.1002/2016JD026403>
- Witte, J. C., Thompson, A. M., Smit, H. G. J., Vömel, H., Posny, F., & Stübi, R. (2018). First reprocessing of southern hemisphere additional ozonesondes profile records: 3. Uncertainty in ozone profile and total column. *Journal of Geophysical Research*, 123(6), 3243–3268. <https://doi.org/10.1002/2017JD027791>
- Wu, L., Mallet, V., Bocquet, M., & Sportisse, B. (2008). A comparison study of data assimilation algorithms for ozone forecasts. *Journal of Geophysical Research*, 113(D20). <https://doi.org/10.1029/2008JD009991>
- Yamashita, Y., Takigawa, M., Ishijima, K., Akiyoshi, H., Kodama, C., Yashiro, H., & Satoh, M. (2017). Resolution dependency of numerically simulated stratosphere-to-troposphere transport associated with mid-latitude closed cyclones in early spring around Japan. *SOLA*, 13, 186–191. <https://doi.org/10.2151/sola.2017-034>
- Yienger, J. J., & Levy, H. (1995). Empirical model of global soil-biogenic NO_x emissions. *Journal of Geophysical Research*, 100(D6), 11447–11464. <https://doi.org/10.1029/95JD00370>
- Zhang, X., Jones, D. B. A., Keller, M., Walker, T. W., Jiang, Z., Henze, D. K., & Rochon, Y. J. (2019). Quantifying emissions of CO and NO_x using observations from MOPITT, OMI, TES, and OSIRIS. *Journal of Geophysical Research*, 124(2), 1170–1193. <https://doi.org/10.1029/2018JD028670>
- Zheng, B., Chevallier, F., Yin, Y., Ciais, P., Fortems-Cheiney, A., Deeter, M. N., & Zhao, Y. (2019). Global atmospheric carbon monoxide budget 2000–2017 inferred from multi-species atmospheric inversions. *Earth System Science Data*, 11(3), 1411–1436. <https://doi.org/10.5194/essd-11-1411-2019>
- Ziskin, D. (2016). MOPITT level 2 derived CO (near and thermal infrared radiances) HDF file – version 7. NASA Langley Atmospheric Science Data Center DAAC. https://doi.org/10.5067/TERRA/MOPITT/MOP02J_L2.007
- Zupanski, D., & Zupanski, M. (2006). Model error estimation employing an ensemble data assimilation approach. *Monthly Weather Review*, 134(5), 1337–1354. <https://doi.org/10.1175/MWR3125.1>
- Zyrichidou, I., Koukouli, M., Balis, D., Markakis, K., Poupkou, A., Katragkou, E., & van Roozendael, M. (2015). Identification of surface NO_x emission sources on a regional scale using OMI NO₂. *Atmospheric Environment*, 101, 82–93. <https://doi.org/10.1016/j.atmosenv.2014.11.023>